

1 SARS-CoV-2 Alpha, Beta and Delta variants display enhanced Spike-mediated 2 Syncytia Formation

3

4 Maaran Michael Rajah^{1,2}, Mathieu Hubert^{1,3,#}, Elodie Bishop^{1,4,#}, Nell Saunders^{1,#}, Remy
5 Robinot¹, Ludivine Grzelak^{1,2}, Delphine Planas^{1,3}, Jérémy Dufloo^{1,2}, Stacy Gellenoncourt^{1,2}, Alice
6 Bongers^{1,2}, Marija Zivaljic^{5,6}, Cyril Planchais⁷, Florence Guivel-Benhassine¹, Françoise Porrot¹,
7 Hugo Mouquet⁷, Lisa Chakrabarti¹, Julian Buchrieser^{1*} Olivier Schwartz^{1,2*}.

8

9 ¹Virus & Immunity Unit, Department of Virology, Institut Pasteur; CNRS UMR 3569, Paris,
10 France

11 ²Université de Paris, Sorbonne Paris Cité, Paris, France

12 ³Vaccine Research Institute, Creteil, France

13 ⁴ Sorbonne Université, Paris F-75005, France⁵Integrative Neurobiology of Cholinergic Systems,
14 Department of Neuroscience, Institut Pasteur; CNRS UMR 3571, Paris, France

15 ⁶Sorbonne Université, ED3C “Brain, cognition, behavior”, Paris, France

16 ⁷Laboratory of Humoral Immunology, Department of Immunology, Institut Pasteur, INSERM
17 U1222, Paris, France

18 # Second co-authors

19 *Last co-authors

20 Corresponding authors: julian.buchrieser@pasteur.fr; olivier.schwartz@pasteur.fr

21 **Abstract**

22 Severe COVID-19 is characterized by lung abnormalities, including the presence of syncytial
23 pneumocytes. Syncytia form when SARS-CoV-2 spike protein expressed on the surface of
24 infected cells interacts with the ACE2 receptor on neighbouring cells. The syncytia forming
25 potential of spike variant proteins remain poorly characterized. Here, we first assessed Alpha
26 and Beta spread and fusion in cell cultures. Alpha and Beta replicated similarly to D614G
27 reference strain in Vero, Caco-2, Calu-3 and primary airway cells. However, Alpha and Beta
28 formed larger and more numerous syncytia. Alpha, Beta and D614G fusion was similarly
29 inhibited by interferon induced transmembrane proteins (IFITMs). Individual mutations present
30 in Alpha and Beta spikes differentially modified fusogenicity, binding to ACE2 and recognition
31 by monoclonal antibodies. We further show that Delta spike also triggers faster fusion relative
32 to D614G. Thus, SARS-CoV-2 emerging variants display enhanced syncytia formation.

33

34

35

36

37

38

39

40 **Synopsis**

41 The Spike protein of the novel SARS-CoV-2 variants are comparative more fusogenic than the earlier
42 strains. The mutations in the variant spike protein differential modulate syncytia formation, ACE2
43 binding, and antibody escape.

- 44 • The spike protein of Alpha, Beta and Delta, in the absence of other viral proteins, induce more
45 syncytia than D614G
- 46 • The ACE2 affinity of the variant spike proteins correlates to their fusogenicity
- 47 • Variant associated mutations P681H, D1118H, and D215G augment cell-cell fusion, while
48 antibody escape mutation E484K, K417N and Δ 242-244 hamper it.
- 49 • Variant spike-mediated syncytia formation is effectively restricted by IFITMs

50 Introduction

51 SARS-CoV-2 was initially discovered during an outbreak in Wuhan, China, before it
52 became pandemic (Huang *et al*, 2020a). Since its emergence, the ancestral Wuhan strain has
53 been supplanted by variants harboring a variety of mutations. Several of these mutations occur
54 in the highly antigenic Spike (S) protein which endowed many of the variants with the ability to
55 evade part of the neutralizing antibody response (Liu *et al*, 2021c; Planas *et al*, 2021a; Rees-
56 Spear *et al*, 2021; Starr *et al*, 2021; Weisblum *et al*, 2020). Individual amino-acid changes in the
57 S protein also affect viral fitness. One of the earliest identified variants contained the D614G
58 mutation in S protein, which increased infectivity without significantly altering antibody
59 neutralization (Yurkovetskiy *et al*, 2020). Several other variants have since emerged and have
60 become globally dominant, including Alpha (B.1.1.7) first identified in the United Kingdom, Beta
61 (B.1.351) identified in South Africa, Gamma (P.1 & P.2) identified in Brazil, and Delta
62 (B.1.617.2) identified in India (Buss *et al*, 2021; Frampton *et al*, 2021; Planas *et al*, 2021b;
63 Sabino *et al*, 2021; Tegally *et al*, 2020; Yadav *et al*, 2021). Some variants are more transmissible
64 but their impact on disease severity is debated (Davies *et al*, 2021; Kemp *et al*, 2021; Korber *et*
65 *al*, 2020).

66 Clinically, SARS-CoV-2 infections range from asymptomatic or febrile respiratory
67 disorders to severe lung injury characterized by vascular thrombosis and alveolar damage
68 (Bussani *et al*, 2020). The deterioration of respiratory tissue is likely a result of both virus-
69 induced cytopathicity and indirect immune-mediated damage (Buchrieser *et al*, 2020; Zhang *et*
70 *al*, 2020; Zhou *et al*, 2020; Zhu *et al*, 2020). A peculiar dysmorphic cellular feature is the

71 presence of large infected multinucleated syncytia; predominately comprised of pneumocytes
72 (Braga *et al*, 2021; Bussani *et al.*, 2020; Sanders *et al*, 2021). Other coronaviruses including
73 SARS-CoV-1, MERS-CoV, and HKU1 also induce syncytia formation in patient tissues and cell
74 culture systems (Chan *et al*, 2013; Dominguez *et al*, 2013; Franks *et al*, 2003; Qian *et al*, 2013).
75 Syncytial cells may compound SARS-CoV-2 induced cytopathicity, play a role in viral persistence
76 and dissemination and could be a pathological substrate for respiratory tissue damage (Braga *et*
77 *al.*, 2021; Buchrieser *et al.*, 2020; Sanders *et al.*, 2021). Release of syncytial cells may contribute
78 to the overall infectious dose (Beucher *et al*, 2021). Heterocellular syncytia containing
79 lymphocytes have also been documented in the lungs of infected patients (Zhang *et al*, 2021).

80 The SARS-CoV-2 S protein is a viral fusogen. The interaction of trimeric S with the ACE2
81 receptor and its subsequent cleavage and priming by surface and endosomal proteases results
82 in virus-cell fusion (Hoffmann *et al*, 2020). Merging of viral and cellular membranes allows for
83 viral contents to be deposited into the cell to begin the viral life cycle. Within the cell, newly
84 synthesized spike, envelope and membrane proteins are inserted into the endoplasmic
85 reticulum (ER), and trafficked and processed through the ER-Golgi network (Cattin-Ortolá *et al*,
86 2021; Duan *et al*, 2020; Nal *et al*, 2005). Virion are formed by budding into ER-Golgi membranes
87 and are then transported to the surface in order to be released from the cell (Klein *et al*, 2020).
88 While the majority of the S protein is sequestered within the ER, motifs within its cytoplasmic
89 tail allow for leakage from the Golgi apparatus and localization at the plasma membrane
90 (Cattin-Ortolá *et al.*, 2021). The S protein at the surface of an infected cell interacts with
91 receptors on adjacent cells, fusing the plasma membranes together and merging the

92 cytoplasmic contents. We and others had previously shown that the S protein interacting with
93 the ACE2 receptor induces cell-cell fusion (Braga *et al.*, 2021; Buchrieser *et al.*, 2020; Lin *et al.*,
94 2021; Sanders *et al.*, 2021; Zhang *et al.*, 2021). The TMPRSS2 protease further augments cell-cell
95 fusion (Barrett *et al.*, 2021; Buchrieser *et al.*, 2020; Hornich *et al.*, 2021).

96 The S protein is comprised of S1 and S2 subunits. The S1 subunit includes the N-terminal
97 domain (NTD) and the receptor binding domain (RBD). The function of the NTD has yet to be
98 fully elucidated but it may be associated with glycan binding, receptor recognition and pre-
99 fusion-to-post fusion conformational changes. The NTD is also targeted by neutralizing
100 antibodies (Chi *et al.*, 2020; Krempl *et al.*, 1997; Zhou *et al.*, 2019). The RBD interacts with the
101 ACE2 receptor and is the main target for neutralizing antibodies (Huang *et al.*, 2020b). The S2
102 domain consists of the fusion peptide (FP), heptapeptide repeat sequences 1 and 2, (HR1 and
103 HR2), the transmembrane anchor, and the C-terminal domain. The FP inserts into the target
104 membrane by disrupting the lipid bilayer and anchors the target membrane to the fusion
105 machinery (Huang *et al.*, 2020b). This exposes regions of HR1 that interact with HR2, forming a
106 flexible loop that brings the membranes together to facilitate fusion (Huang *et al.*, 2020b). The
107 versatility of the S protein suggests that any mutations that have arisen are of particular
108 concern as they can affect fusogenicity, antibody recognition, affinity to ACE2, proteolytic
109 processing and incorporation into virions. There is a general paucity of information regarding
110 how the mutations associated with variant S proteins contribute to cell-cell fusion.

111 S-mediated cell-cell fusion is sensitive to innate immunity components. The interferon
112 response to SARS-CoV-2 is one of the key factors down-modulating viral entry and replication,

113 and deficiencies in the interferon response are associated with severe or critical COVID-19
114 (Arunachalam *et al*, 2020; Bastard *et al*, 2021; Bastard *et al*, 2020; Hadjadj *et al*, 2020; van der
115 Made *et al*, 2020). SARS-CoV-2 induced syncytia formation by the Wuhan strain is restricted by
116 innate immunity, in part through the action of interferon induced transmembrane proteins
117 (IFITMs) (Buchrieser *et al.*, 2020). IFITM1, 2 and 3 are restriction factors which display antiviral
118 activity against a variety of enveloped viruses including SARS-CoV-2; likely by increasing
119 membrane rigidity and hindering virus-cell fusion (Shi *et al*, 2021). Their effectiveness at
120 restricting cell-cell fusion of novel variants has yet to be assessed.

121 Here, we compared the replication and syncytia forming potential of D614G, Alpha and
122 Beta viruses in human cell lines and primary airway cells. We further characterized the
123 fusogenicity of the Alpha and Beta variant S proteins and the individual contribution of each of
124 the component mutations in syncytia formation, ACE2 binding and evasion from a panel of
125 antibodies. Finally, we examined the syncytia forming potential and ACE2 binding capacity of
126 the novel Delta variant spike.

127

128 **Results**

129 **Comparative Replication Kinetics of SARS-CoV-2 Variants**

130 We compared the replication kinetics of SARS-CoV-2 variants in relevant cell cultures.
131 We first infected Caco-2, Calu-3 and Vero cells with Alpha, Beta, and D614G variants and
132 generated multistep growth curves (**Fig. 1**). Cell were infected at an equivalent, non-saturating

133 MOI, initially titrated in Vero cells (**Fig. EV1A**). Viral replication was assessed at 24, 48, and 72
134 hours by flow cytometry upon staining with the pan-SARS-CoV-2 anti-S mAb102 human
135 monoclonal antibody (Planas *et al.*, 2021a) and then gating for S+ cells (**Fig. EV1B**). Globally, the
136 variants replicated similarly (**Fig. 1**). This similar replication was observed at different MOIs (**Fig.**
137 **EV1A**). There were subtle differences at 24h post-infection, depending on the cell line and the
138 variant. For instance, Beta replicated slightly more than D614G in Caco-2 cells whereas Alpha
139 replicated slight less than D614G in Vero cells (**Fig. 1A, C**). Viral release at each time point was
140 also assessed by extracting RNA from the supernatant and performing RT-qPCR for the gene
141 encoding the N protein. Viral release was again roughly similar with the different variants,
142 especially at early time points. Alpha produced moderately more virus than D614G in all cell
143 lines at later time points (**Fig. 1A-C**). Beta produced more virus than D614G in Caco-2 but less in
144 Calu-3 cells at later time points (**Fig. 1A, B**).

145 We then used the MucilAirB™ model, which consists of primary human airway epithelial
146 cells (HAEC) grown over a porous membrane and differentiated at the air-liquid interface for
147 over 4 weeks. This relevant model is susceptible to SARS-CoV-2 infection (Pizzorno *et al.*, 2020;
148 Robinot *et al.*, 2020; Robinot *et al.*, 2021; Touret *et al.*, 2021). The cells were infected with each
149 variant at a similar low viral inoculum (10^4 TCID50). Viral RNA and infectious virus release were
150 monitored over 96h by RT-qPCR and TCID50. Alpha and Beta variants produced slightly more
151 extracellular viral RNA than D614G at later time points but not significantly higher levels of
152 infectious particles (**Fig. 1D**).

153 Taken together our data show that Alpha and Beta variants replicate similarly to the
154 ancestral D614G strain in a panel of human cell lines and in primary cells, with some slight
155 differences.

156 **Syncytia formation in cells infected with SARS-CoV-2 variants.**

157 We next assessed the potential of SARS-CoV-2 variants to induce syncytia. In order to
158 visualize cell-cell fusion, we employed our previously described S-Fuse assay, using U2OS-ACE2
159 GFP-split cells (Buchrieser *et al.*, 2020). In the GFP-split complementation system, two cell lines
160 containing half of the reporter protein are co-cultured, producing a GFP signal only upon fusion
161 **(Fig. 2A)**. Upon infection of S-Fuse cells, we noticed that the Alpha and Beta variants formed
162 larger and more numerous infected syncytia than either D614G or the ancestral Wuhan strain
163 **(Fig. EV2A)**. We then characterized quantitatively the differences in fusogenicity by calculating
164 the total syncytia (GFP) area and then normalizing it to nuclei number (Hoechst) **(Fig. EV2B)**.
165 Relative to D614G, Alpha and Beta variants produced significantly more syncytia, approximately
166 4.5 and 3-fold respectively, after 20h of infection with the same MOI **(Fig. 2B and EV3A)**. In
167 order to characterize syncytia formation in a cell line expressing endogenous ACE2, we
168 generated Vero cells carrying the GFP-split system. After 48h of infection with the same MOI,
169 we again found that Alpha and Beta variants produced significantly more syncytia than D614G
170 **(Fig. 2C and EV3B)** despite similar infection levels **(Fig. 1C)**. Of note, D614G produced similar
171 levels of syncytia as the Wuhan strain in both Vero and S-Fuse cells **(Fig. 2 and EV3A-B)**.

172 Therefore, Alpha and Beta variants appear more fusogenic than D614G in S-Fuse and
173 Vero cells.

174

175 **Syncytia formation in cells expressing variant Spikes.**

176 Since syncytia formation is a consequence of the S protein expressed on the surface of
177 an infected cell interacting with ACE2 receptors on neighboring cell, we sought to compare the
178 fusogenic potential of the individual variant S proteins. We introduced the D614G mutation into
179 the Wuhan protein and designed plasmids to express Alpha and Beta S proteins. We
180 transfected the respective plasmids into Vero GFP-split cells and quantified syncytia formation
181 18h later (**Fig. 3A**). Alpha and Beta S proteins were 2 and 1.7-fold more fusogenic than D614G S,
182 respectively (**Fig. 3B**). The Wuhan S was slightly less fusogenic than the D614G S (**Fig. 3B**). We
183 then verified that the variation in S mediated fusion was not due to differential cell surface
184 levels. We transfected 293T cells, which lack ACE2 and thus do not fuse upon S expression, with
185 the different variant plasmids in order to assess S protein surface levels by flow cytometry. The
186 variants S proteins were equally expressed after transfection (**Fig. EV4A-C**).

187 We then measured the kinetics of syncytia formation induced by the different S proteins
188 in Vero GFP-Split cells. We conducted a comparative video-microscopy analysis where cell-cell
189 fusion could be visualized as soon as 6h post-transfection. The fusion kinetics of Alpha S protein
190 was more rapid than any of the other variants (**Fig. 3C and Movie E1**). Beta also induced
191 significantly faster fusion than D614G, whereas the Wuhan S was the slowest of all the
192 compared proteins (**Fig. 3C and Movie E1**).

193 We then asked whether the TMPRSS2 protease, that cleaves S and facilitate viral fusion,
194 may act differently on the variant S proteins. To this aim, we expressed the different variant S
195 proteins without or with TMPRSS2 in 293T cells. We examined the processing of the different S
196 by western blot and the surface levels by flow cytometry. The cleavage profile induced by
197 TMPRSS2 and the surface levels of the different variant S proteins were similar (**Fig EV4E**).

198 Altogether, our data indicate that the S proteins of Alpha and Beta variants form more syncytia
199 than D614G or Wuhan strains.

200 **Restriction of S mediated syncytia formation by IFN- β 1 and IFITMs.**

201 As the variants did not show any major difference in replication under basal conditions,
202 we next investigated if they were differently sensitive to the interferon response. To this aim,
203 we pre-treated Vero cells or U2OS-ACE2 (S-Fuse) cells with increasing doses of IFN- β 1 and
204 infected them with the different variants. IFN- β 1 was equally effective at reducing viral
205 replication of D614G, Alpha, and Beta variants in Vero cells (**Fig. EV5A**). Preincubation of S-Fuse
206 cell with IFN- β 1 also abrogated infection and syncytia formation to the same extent with the
207 different variants (**Fig. EV5B**). Therefore, IFN- β 1 similarly inhibited viral replication and reduced
208 syncytia formation by D614G, Alpha and Beta variants.

209 IFITMs are interferon stimulated transmembrane proteins that restrict early stages of the viral
210 life cycle by inhibiting virus-cell fusion; likely by modifying the rigidity or curvature of
211 membranes (Compton *et al*, 2014; Shi *et al*, 2017; Zani & Yount, 2018). IFITM1 localizes at the
212 plasma membrane while IFITM2 and 3 transit through surface and localize in endo-lysosomal

213 compartments (Buchrieser *et al.*, 2020). We previously reported that IFITMs restrict Wuhan S
214 mediated cell-cell fusion and that their activity was counteracted by the TMPRSS2 protease
215 (Buchrieser *et al.*, 2020). As infection with Alpha and Beta induce more syncytia, we further
216 investigated if this resulted in an increased resistance to IFITM restriction. We thus
217 characterized the impact of IFITMs on syncytia formed upon expression of D614G, Alpha and
218 Beta S proteins in 293T cells. The variants were effectively restricted by IFITMs (**Fig. EV5C-G**). Of
219 note, the three IFITMs were expressed at similar levels (not shown). The presence of TMPRSS2
220 increased fusion of all S proteins and reverted the restriction by IFITMs (**Fig. EV5C-G**). Taken
221 together, our data show that Alpha and Beta variants induce more syncytia, but their S proteins
222 remain similarly sensitive to IFITMs.

223

224 **Contribution of individual variant-associated mutations on Spike fusogenicity.**

225 We next sought to determine the contribution of each variant-associated mutation to
226 cell-cell fusion. Both Alpha and Beta S proteins contain the N501Y mutation in the RBD and the
227 D614G mutation in the S1/S2 cleavage site (**Fig. 4A**). Alpha S contains the $\Delta 69/70$ and $\Delta Y144$
228 deletions in the N-terminal domain (NTD), P681H and T716I mutations in the S1/S2 cleavage
229 site, the S982A mutation in the heptad repeat 1 (HR1) site and the D1118H mutation in
230 between HR1 and HR2. The Beta S is comprised of the L18F, D80A, D215G and $\Delta 242-244$
231 mutations in the NTD, K417N and E484K mutations in the receptor binding domain (RBD), and
232 A701V in the S1/S2 cleavage site. We introduced individual mutations into the D614G
233 background. Following reports of the emergence of the E484K mutation within the Alpha

234 variant (Collier *et al*, 2021), we also generated a mutant Alpha S protein with the E484K
235 mutation. We observed by flow cytometry that the mutant S proteins were similarly expressed
236 at the cell surface (**Fig. EV4A-C and EV6 A-D**). We expressed each mutant into Vero GFP split
237 and measured their potential to induce cell-cell fusion in comparison to D614G S protein.

238 Of the mutations that are associated with Alpha, we found that the $\Delta 69/70$ deletion in
239 the RBD decreased cell-cell fusion whereas P681H and D1118H substitutions both increase
240 fusion (**Fig. 4A and EV6G**). P681H displayed the greatest fusogenicity of all investigated
241 mutations, being almost 2.5-fold higher than D614G S (**Fig. 4A and EV6G**). As previously
242 mentioned, the introduction of the D614G mutation in the S1/S2 border of the Wuhan S
243 protein also relatively increased fusion, stressing the importance of this cleavage site in
244 fusogenicity (**Fig. 3B**).

245 Among the mutations associated with Beta, the $\Delta 242-244$ deletion, as well as K417N
246 and E484K mutations in the RBD significantly decreased syncytia formation (**Fig. 4A and EV6H**).
247 Only the D251G mutation in the NTD modestly increased syncytia formation relative to D614G
248 (**Fig. 4A and EV6H**). The introduction of the E484K RBD mutation into the Alpha S protein
249 significantly decreased its potential to form syncytia, despite not changing cell surface
250 expression, further supporting the mutation's restrictive effect on cell-cell fusion (**Fig. 4B and**
251 **EV4B**). Taken together, our data suggests that variant S proteins are comprised of mutations
252 that play contrasting roles in cell-cell fusion. P681H, D1118H, and D215G substitutions facilitate
253 fusion, whereas mutations $\Delta 69/70$, $\Delta 242-244$, K417N, and E484K antagonize cell-cell fusion.

254

255 **Binding of S proteins bearing individual variant-associated mutations to ACE2.**

256 We next explored the impact of variant-associated mutations on S binding to the ACE2
257 receptor. To this aim, we transiently expressed each mutant protein in 293T cells. Cells were
258 then stained with a serial dilution of soluble biotinylated ACE2, revealed with fluorescent
259 streptavidin and then analyzed by flow cytometry (**Fig. 5A**). Titration binding curves were
260 generated and EC50 (the amount of ACE2 needed for 50% binding) was calculated. The S
261 protein of Alpha had the highest affinity to ACE2, confirming previous results by us and others
262 (Planas *et al.*, 2021)(Ramanathan *et al.*, 2021). Alpha was sequentially followed by Beta, D614G,
263 and Wuhan S (**Fig. 5B and EV7A**). As expected, mutations within the RBD had the most
264 significant impact on ACE2 binding. N501Y found in both Alpha and Beta drastically increased
265 ACE2 binding, in line with previous reports indicating that this mutation enhances affinity of the
266 viral protein to its receptor (Ali *et al.*, 2021; Luan *et al.*, 2021; Tian *et al.*, 2021). The K417N
267 substitution present in the Beta S decreased ACE2 binding (**Fig. 5B and EV7C**). The E484K
268 mutant had a slightly, but not significantly, higher binding to ACE2 (**Fig. EV7C**). This was
269 corroborated by the observation that addition of the E484K mutation to Alpha S protein also
270 slightly increased ACE2 binding (**Fig. 5B and EV7A**). Mutation in the S1/S2 cleavage site,
271 HR1/HR2 sites or NTD did not have any significant impact on ACE2 binding (**Fig. 5B and EV7B-E**).
272 It is worth noting that the NTD Δ 242-244 mutant displayed a marginally lower binding to ACE2
273 (**Fig. 5B and EV7B**). Therefore, the N501Y mutation is the most significant contributor to
274 increased ACE2 binding of the variants, though it does not affect cell-cell fusion on its own. The

275 K417N, Δ 242-244, and E484K mutations restrict fusogenicity but differently effect ACE2
276 binding; with the former two decreasing affinity and the latter slightly increasing.

277 Therefore, ACE2 binding and fusogenicity are two functions of the S protein that can be
278 partially deconvoluted through individual mutations.

279

280 **Antibody binding to S proteins bearing individual variant-associated mutations.**

281 We had previously found that certain neutralizing antibodies differentially affect SARS-
282 CoV-2 D614G, Alpha and Beta variants (Planas *et al.*, 2021a). For instance, neutralizing
283 monoclonal antibody 48 (mAb48) restricts D614G virus but not Alpha or Beta variants (Planas *et*
284 *al.*, 2021a). We sought to determine which mutations in variant S proteins contributed to the
285 lack of recognition by the neutralizing antibodies. To this aim, we assessed by flow cytometry
286 the binding of a panel of four human monoclonal antibodies (mAbs) to the different S mutants.
287 As a control we used mAb10, a pan-coronavirus antibody that targets an unknown but
288 conserved epitope within the S2 region (Planchais, manuscript in preparation). mAb10 equally
289 recognized all variants and associated individual mutations (**Fig. 5C**). mAb48 and mAb98 target
290 the RBD and mAb71 the NTD (Planas *et al.*, 2021b)(Planchais, manuscript in preparation).
291 mAb48 did not recognize the Beta variant, and more specifically did not bind to the K417N
292 mutant (**Fig. 5C**). The mAb71 recognized neither Alpha nor Beta variants and did not bind to
293 their respective NTD Δ Y144 and Δ 242-244 mutations. The K417N and Δ 242-244 mutations were
294 also responsible for decreasing S-mediated fusion, suggesting a tradeoff between antibody

295 escape and fusion (**Fig. 5C**). mAb98 did not recognize the Beta variant. However, none of the
296 associated mutations were specifically responsible for the lack of binding (**Fig. 5C**), suggesting a
297 combined effect on the structure of the S protein that may affect antibody escape.

298 Therefore, several of the mutations found in the variants spike proteins are
299 advantageous in terms of antibody escape despite slightly reducing the ability the proteins to
300 fuse.

301 **Spike mediated syncytia formation by the Delta variant.**

302 With the emergence and rapid spread of the Delta variant, we sought to characterize its
303 potential to form syncytia. We recently showed that the Delta variant induce large syncytia in S-
304 Fuse cells (Planas *et al.*, 2021b). We thus compared the fusogenicity of the Delta S protein to
305 that of D614G and Alpha. We transiently expressed the three S proteins in Vero-GFP split cells.
306 The Delta S protein triggered more cell-cell fusion than the D614G variant but was similar to the
307 Alpha S protein (**Fig 6A**). The fusion kinetic of the Delta S was also similar to Alpha but more
308 rapid than D614G (**Fig 6B**). We confirmed that the variant S proteins were equally expressed on
309 the surface by transfecting them into non-fusogenic 293T cells and performing flow cytometry
310 upon staining with the pan-SARS-CoV-2 mAb129 (**Fig EV4D**). We next examined the ACE2
311 binding potential of Delta S protein using our aforementioned soluble biotinylated ACE2. The
312 Delta S protein has a higher binding capacity to ACE2 than the D614G S protein, but the binding
313 was lower than the Alpha S protein (**Fig 6C**).

314

315 Discussion

316 The replication and cytopathic effects of SARS-CoV-2 variants is under intense scrutiny,
317 with contrasting results in the literature (Frampton *et al.*, 2021; Hou *et al.*, 2020; Leung *et al.*,
318 2021; Liu *et al.*, 2021b; Touret *et al.*, 2021). For instance, there was no major difference in the
319 replication kinetics of Alpha and D614G strains in some reports (Thorne *et al.*, 2021; Touret *et*
320 *al.*, 2021), whereas others suggested that Alpha may outcompete D614G in a co-infection assay
321 (Touret *et al.*, 2021). Other studies proposed that the N501Y mutation may provide a
322 replication advantage, whereas others suggested that N501Y is deleterious (Frampton *et al.*,
323 2021; Hou *et al.*, 2020; Leung *et al.*, 2021; Liu *et al.*, 2021b). These discrepant results may be
324 due to the use of different experimental systems, viral strains, multiplicities of infection and cell
325 types.

326 Here, we show that Alpha and Beta variants replicate to the same extent as the early
327 D614G strain in different human cell lines and primary airway cells. Moreover, Alpha and Beta
328 induced more cell-cell fusion than D614G. Increased fusion was observed in U2OS-ACE2 cells
329 and in naturally permissive Vero cells. In agreement with infection data, transfection of Alpha
330 and Beta S proteins, in the absence of any other viral factors, produced significantly more
331 syncytia than D614G, which in turn, fused more than the Wuhan S. Comparative video
332 microscopy analysis revealed that Alpha S fused the most rapidly, followed by Beta, D614G, and
333 finally Wuhan. Thus, Alpha and Beta variants display enhanced S-mediated syncytia formation.

334 We further show that Alpha and Beta remain sensitive to restriction by IFN- β 1. The
335 fusion mediated by their respective S proteins is inhibited by IFITMs. This extends previous

336 results by us and others demonstrating that ancestral Wuhan S is effectively inhibited by this
337 family of restriction factors (Buchrieser *et al.*, 2020; Shi *et al.*, 2021). It has been recently
338 reported in a pre-print that Alpha may lead to lower levels of IFN- β 1 production by infected
339 Calu-3 cells and may be less sensitive to IFN- β pre-treatment, when compared to first wave viral
340 isolates (Thorne *et al.*, 2021). We did not detect here differences of IFN- β 1 sensitivity between
341 the variants in Vero and U2OS-ACE2 cells. Again, these discrepant results may reflect inherent
342 differences between Calu-3, Vero and U2OS-ACE2 cells, or the use of different viral isolates.

343 We then characterized the contribution of the individual mutations present in Alpha and
344 Beta S proteins to their respective fusogenicity. The highly fusogenic Alpha S consists of more
345 mutations that robustly increase fusion (P681H and D1118H) than mutations that decrease
346 fusion (Δ 69/70). In contrast, the Beta variant is comprised of several restrictive mutations
347 (Δ 242-244, K417N, and E484K) and only one mutation that modestly increased fusion (D215G).
348 The strongest increase in fusion was elicited by the P681H mutation at the S1/S2 border. This
349 mutation likely facilitates proteolytic cleavage of S and thus promotes S mediate cell-cell fusion.
350 Indeed, the analogous P681R mutation present in B.1.617.2 and B.1.617.3 variants increases
351 S1/S2 cleavage and facilitates syncytia formation (Ferreira *et al.*, 2021; Jiang *et al.*, 2020). Of
352 note, another report with indirect assessment of variant S fusogenicity suggested a mild
353 decrease or no difference in cell-cell fusion of Alpha and Beta relative to Wuhan S (Hoffmann *et*
354 *al.*, 2021). These previous experiments were performed in 293T cells at a late time-points (24
355 hours post-transfection), which may preclude detection of an accelerated fusion triggered by
356 the variants.

357 We show that the binding of variant S to soluble ACE2 paralleled their fusogenicity.
358 Alpha bound the most efficiently to ACE2, followed by Beta, D614G and finally Wuhan.
359 However, the ACE2 affinity of S proteins carrying individual mutations did not exactly correlate
360 to fusogenicity. For instance, the N501Y and D614G mutations drastically increased ACE2
361 affinity, but only D614G enhanced fusogenicity. The K417N substitution, and to a lesser degree
362 Δ 242-244, had a lower affinity to ACE2 and also restricted cell-cell fusion. The E484K mutation
363 significantly restricts fusion, but mildly increases ACE2 affinity. This suggests that on the level of
364 individual S mutations, the relationship between ACE2 affinity and increased fusogenicity is not
365 always linear. Variant mutations may also confer advantages in an ACE2 independent manner.
366 Indeed, recent work has suggested that the E484 mutation may facilitate viral entry into H522
367 lung cells, requiring surface heparan sulfates rather than ACE2 (Puray-Chavez *et al*, 2021). It
368 would be of future interest to examine the syncytia formation potential of the variant
369 mutations in other cell types.

370 We selected a panel of 4 mAbs that displayed different profiles of binding to Alpha,
371 Beta, D614G and Wuhan S proteins. The mAb10 targeting the S2 domain recognized all variants
372 and was used as a positive control. Wuhan and D614G were recognized by the three other
373 antibodies, targeting either the NTD or RBD. Alpha lost recognition by the anti-NTD mAb71,
374 whereas Beta was neither recognized by mab71 nor by the two anti-RBD antibodies mAb48 and
375 mAb 98. Upon examining the potential of S proteins carrying individual mutations to bind to
376 human monoclonal antibodies, we found that the ones that restrict (Δ 242-244, K417N) or have
377 no effect on fusogenicity (Δ Y144) are also not recognized by some mAbs. This suggests that

378 variant S proteins have undergone evolutionary trade off in some circumstances; selecting for
379 mutations that provide antibody escape at the detriment of fusogenicity. In accordance with
380 our findings, deep sequence binding analysis and in vitro evolution studies suggest the N501Y
381 mutation increases affinity to ACE2 without disturbing antibody neutralization (Liu *et al*, 2021a;
382 Starr *et al.*, 2021; Zahradník *et al*, 2021). The E484K and K417N RBD mutations in the Beta
383 variant may also increase ACE2 affinity, particularly when in conjunction with N501Y (Zahradník
384 *et al.*, 2021) (Nelson *et al*, 2021). However, the resulting conformational change of the S protein
385 RBD may also decrease sensitivity to neutralizing antibodies (Nelson *et al.*, 2021). Future work
386 assessing the structural and conformational changes in the S protein elicited by a combination
387 of individual mutations or deletions may further help elucidate the increased fusogenicity and
388 antibody escape potential of the variants.

389 While we had previously shown that the interaction between the S protein on the
390 plasma membrane with the ACE2 receptor on neighboring cells is sufficient to induce syncytia
391 formation, there is compelling evidence of the importance of the TMPRSS2 protease in S
392 activation (Buchrieser *et al.*, 2020; Dittmar *et al*, 2021; Koch *et al*, 2021; Ou *et al*, 2021). We did
393 not detect any major differences in the processing of the variant spike proteins by TMPRSS2. It
394 will be worth further characterizing how the fusogenicity of variant associated mutations are
395 influenced by other cellular proteases.

396 The presence of infected syncytial pneumocytes was documented in the lungs of
397 patients with severe COVID-19 (Bussani *et al.*, 2020; Tian *et al*, 2020; Xu *et al*, 2020). Syncytia
398 formation may contribute to SARS-CoV-2 replication and spread, immune evasion and tissue

399 damage. A report using reconstituted bronchial epithelia found that viral infection results in the
400 formation and release of infected syncytia that contribute to the infectious dose (Beucher *et al.*,
401 2021). The neutralizing antibody response to SARS-CoV-2 infection has divergent effect on cell-
402 cell fusion, with some antibodies restricting S mediated fusion, while other increase syncytia
403 formation (Asarnow *et al.*, 2021). Cell-to-cell spread of virus may be less sensitive to
404 neutralization by monoclonal antibodies and convalescent plasma than cell-free virus (Jackson
405 *et al.*, 2021). It is thus possible that infected syncytial cells facilitate viral spread. Within this
406 context, it is necessary to better understand the fusogenic potential of the SARS-CoV-2 variants
407 that have arisen and will continue to emerge.

408 We have characterized here the replication, fusogenicity, ACE2 binding and antibody
409 recognition of Alpha and Beta variants and the role of their S-associated mutations. Despite the
410 insights we provide into the S-mediated fusogenicity of the variants, we did not address the
411 conformational changes that the mutations individually or in combination may elicit. We
412 further show that Alpha, Beta and Delta spike proteins more efficiently bind to ACE2 and are
413 more fusogenic than D614G. Which virological and immunological features of the Delta variant
414 explain its higher estimated transmissibility rate than Alpha and other variants at the
415 population level remains an outstanding question.

416

417

418

419

420

421

422

423

424 **Material and Methods**

425

426 **Plasmids**

427 A codon optimized version of the reference Wuhan SARS-CoV-2 Spike (GenBank: QHD43416.1)
428 was ordered as a synthetic gene (GeneArt, Thermo Fisher Scientific) and was cloned into a
429 phCMV backbone (GenBank: AJ318514), by replacing the VSV-G gene. The mutations for Alpha
430 and Beta (**Fig. 4A**) were added in silico to the codon-optimized Wuhan strain and ordered as
431 synthetic genes (GeneArt, Thermo Fisher Scientific) and cloned into the same backbone (Planas
432 *et al.*, 2021a). The D614G S-protein was generated by introducing the mutation into the Wuhan
433 reference strain via Q5 Site-directed mutagenesis (NEB). Other individual mutations were
434 subsequently introduced into the D614G S by the same process. Plasmids were sequenced prior
435 to use. The primers used for sequencing and the site-directed mutagenesis are presented in the
436 supplement (**EV Tables 1 and 2**). pQCXIP-Empty control plasmid, pQCXIP-IFITM1-N-FLAG,

437 pQCXIP-IFITM2-N-FLAG, pQCXIP-IFITM3-N-FLAG were previously described (Buchrieser *et al*,
438 2019). pQCXIP-BSR-GFP11 and pQCXIP-GFP1-10 were from Yutaka Hata ((Kodaka *et al*, 2015);
439 Addgene plasmid #68716; <http://n2t.net/addgene:68716>; RRID: Addgene_68716 and Addgene
440 plasmid #68715; <http://n2t.net/addgene:68715>; RRID: Addgene_68715). pcDNA3.1-hACE2 was
441 from Hyeryun Choe ((Li *et al*, 2003); Addgene plasmid # 1786; <http://n2t.net/addgene:1786>;
442 RRID: Addgene_1786). pCSDest-TMPRSS2 was from Roger Reeves ((Edie *et al*, 2018); Addgene
443 plasmid # 53887; <http://n2t.net/addgene:53887>; RRID: Addgene_53887).

444 **Cells**

445 Vero E6, HEK293T, U2OS, Caco2/TC7, Calu3 were cultured in DMEM with 10% Fetal Bovine
446 Serum (FBS) and 1% Penicillin/Streptomycin (PS). Vero and 293T GFP-split cells transduced cells
447 with pQCXIP were cultured with 4ug/ml and 1 ug/ml of puromycin (InvivoGen), respectively.
448 U2OS GFP-split cells transduced with pLenti6 were cultured in 1ug/ml puromycin and 10 ug/ml
449 blasticidin (InvivoGen). The MucilAirTM primary human bronchial epithelial model was
450 previously described (Robinot *et al.*, 2021). All cells lines were either purchased from ATCC or
451 were kind donations from members of the Institut Pasteur and were routinely screened for
452 mycoplasma.

453

454 **Viruses**

455 The Wuhan SARS-CoV-2 strain (BetaCoV/France/IDF0372/2020) and the D614G strain (hCoV-
456 19/France/GE1973/2020) was supplied by Dr. S. van der Werf of the National Reference Centre

457 for Respiratory Viruses (Institut Pasteur, Paris, France). The D614G viral strain was sourced
458 through the European Virus Archive goes Global (EVAg) platform, which is funded by the
459 European Union's Horizon 2020 research and innovation program under grant agreement
460 653316. The Alpha strain was isolated in Tours, France, from an individual who returned from
461 the United Kingdom. The Beta strain (CNRT 202100078) originated from an individual in Creteil,
462 France). Informed consent was provided by the individuals for use of their biological materials.
463 The viruses were isolated from nasal swabs on Vero cells and further amplified one or two
464 passages on Vero cells. The viruses were sequenced directly from the nasal squabs and again
465 upon passaging. Titration of Viral stocks was performed by 50% tissue culture infectious dose
466 (TCID50).

467

468 **Viral Release**

469 For quantification of extracellular viral RNA, supernatants were diluted and heat-inactivated for
470 20min at 80°C. qRT-PCR was performed from 1µL of template RNA in a final volume of 5 µL per
471 reaction in 384-well plates using the Luna Universal Probe One-Step RT-qPCR Kit (New England
472 Biolabs) with SARS-CoV-2 N-specific primers (**EV Table 1**) on a QuantStudio 6 Flex
473 thermocycler (Applied Biosystems). Standard curve was performed in parallel using purified
474 SARS-CoV-2 viral RNA. Infectious virus release was assessed by harvesting supernatant at each
475 time point and performing a TCID50 assay using Vero cells.

476

477 **GFP-Split Fusion assay**

478 For cell-cell fusion assays, Vero, U2OS-ACE2, or 293T cell lines stably expressing GFP1-10 and
479 GFP11 were co-cultured at a 1:1 ration (3×10^4 , 2×10^4 and 7×10^4 cells/well total, respectively)
480 were transfected in suspension with a total of 100ng of DNA with Lipofectamine 2000 (Thermo)
481 in a 96 well plate (uClear, #655090). 10 ng of pHCMV-SARS-CoV2-S and/or 25 ng of pCDNA3.1-
482 hACE2, 25 ng of pCSDest-TMPRSS2, and 40 ng of pQCXIP-IFITM were used and adjusted to 100
483 ng DNA with pQCXIP-Empty (control plasmid). At 20 h post-transfection images covering 80-
484 90% of the well surface, were acquired per well on an Opera Phenix High-Content Screening
485 System (PerkinElmer). The GFP area and the number of nuclei was quantified on Harmony High-
486 Content Imaging and Analysis Software (**Fig EV2B**). For infection, cells were plated at the
487 aforementioned concentrations and infected the next day with a range of MOIs and fixed at
488 20h (U2OS-ACE) or 48h (Vero) post-infection with 4% paraformaldehyde for 30mins. For video
489 microscopy experiments, Vero GFP split cells (mixed 1:1) were transfected in suspension with
490 50ng of pHCMV-SARS-CoV2-S and 450ng of pQCXIP-Empty for 30mins at 37°C. Cells were
491 washed twice and then seeded at a confluency of 2×10^5 cells per quadrant in a u-Dish 35mm
492 Quad dish (ibidi-#80416). Cells were allowed to settle, and fluorescence images were taken at
493 37°C every 10min up to 24h using a Nikon BioStation IMQ, with three fields for each condition.
494 Fusion defined as percent of GFP pixels was calculated with ImageJ.

495

496 **Flow cytometry**

497 For ACE2 binding, 293T cells transfected with S proteins for 24h were stained with soluble
498 biotinylated ACE2 diluted in MACS Buffer at indicated concentrations (from 60 to 0.01 µg/mL)
499 for 30 min at 4°C. The cells were then washed twice with PBS and then incubated with Alexa
500 Fluor 647- conjugated-streptavidin (Thermo Fisher Scientific, 1:400) for 30 min at 4°C. Finally,
501 the cells were washed twice with PBS and then fixed with 4% paraformaldehyde. The results
502 were acquired using an Attune Nxt Flow Cytometer (Life Technologies). Transfection efficiency
503 was assessed by staining with pan-SARS-CoV-2 human mAb129. Antibody binding to S proteins
504 was assessed via a analogous protocol where transfected 293T cells were first stained with
505 either human mAb10 (pan-coronavirus anti-S2), mAb102 and mAb129 (pan-SARS-CoV-2),
506 mAb48 and mAb98 (SARS-CoV-2 anti-RBD), and mAb71 (SARS-CoV-2 anti-NTD) at 1 µg/mL. The
507 antibodies were derived from convalescent individuals by the Mouquet lab at the Institut
508 Pasteur. mAb10 was generated during the early stages of the epidemic from a patient infected
509 with the Wuhan strain and thus has a higher affinity for the Wuhan spike (Planas *et al.*, 2021a).
510 For viral replication, infected cells were fixed at each time with 4% paraformaldehyde for 30
511 mins. The cells were stained in the same manner described above with anti-spike mAb102 and
512 secondary Alexa Fluor 647 (1:500) in MACS buffer containing 0.05% saponin. The gating
513 strategy to determine spike positive cells is represented in the supplement (**Fig EV1B**).

514 **Western Blot**

515 Cells were lysed in TXNE buffer (1% Triton X-100, 50 mM Tris-HCl (pH 7.4), 150 mM NaCl, 5 mM
516 EDTA, protease inhibitors) for 30 min on ice. Equal amounts (20–50 µg) of cell lysates were
517 analyzed by Western blot. The following antibodies were diluted in WB-buffer (PBS, 1% BSA,

518 0.05% Tween, 0.01% Na Azide): rabbit anti-human TMPRSS2 (Atlas antibodies cat# HPA035787,
519 1:1,000), rabbit anti-human actin (Sigma cat#A2066, 1:2,000), and human anti-S Serum derived
520 from a convalescent individual (1:1000). Species-specific secondary DyLight-coupled antibodies
521 were used (diluted 1:10,000 in WB-buffer) and proteins revealed using a Licor Imager. Images
522 were quantified and processed using Image Studio Lite software.

523

524

525 **Statistical analysis**

526 Flow cytometry data was analyzed with FlowJo v10 software (Tristar). Calculations were all
527 performed with Microsoft Excel 365. GraphPad Prism 9 was used to generate figures and for
528 statistical analysis. Statistical significance between different conditions was calculated using the
529 tests indicated in the corresponding figure legends.

530 **Acknowledgments**

531 We thank members of the Virus and Immunity Unit for helpful discussions and Dr. Nicoletta
532 Casartelli for her critical reading of the manuscript. Nathalie Aulner and the UtechS Photonic
533 Biolmaging (UPBI) core facility (Institut Pasteur), a member of the France Biolmaging network,
534 for image acquisition and analysis support. Work in OS lab is funded by Institut Pasteur,
535 Urgence COVID-19 Fundraising Campaign of Institut Pasteur, ANRS, the Vaccine Research
536 Institute (ANR-10-LABX-77), Fondation Pour la Recherche Médicale (FRM), Labex IBEID (ANR-
537 10-LABX62-IBEID), ANR/FRM Flash Covid PROTEO-SARS-CoV-2 and IDISCOVER. Work in UPBI is
538 funded by grant ANR-10-INSB-04-01 and Région Ile-de-France program DIM1-Health. MMR and
539 MZ are supported by the Pasteur-Paris University (PPU) International Doctoral Program. DP is
540 supported by the Vaccine Research Institute. LG is supported by the French Ministry of Higher
541 Education, Research and Innovation. EB is supported by the Medecine-Sciences ENS-PSL
542 Program. HM lab is funded by the Institut Pasteur, the Milieu Intérieur Program (ANR-10-LABX-
543 69- 01), the INSERM, REACTing, EU (RECOVER) and Fondation de France (#00106077) grants.
544 The funders of this study had no role in study design, data collection, analysis, interpretation, or
545 the writing of the article.

546

547 **Author contributions**

548 Experimental strategy and design: MMR, JB, MH, LG, RR, LC, OS.

549 Experimentation: MMR, JB, MH, EB, RR, NS, LG, FGB, FP, RR, JD, SG, AB.

550 Vital materials and expert advice: CP and HM.

551 Data processing and figure generation: MMR.

552 Manuscript writing and editing MMR, JB, OS.

553 Supervision: JB and OS.

554 All authors reviewed and approved the manuscript,

555

556 **Conflict of interests:** CP, HM and OS have a pending patent application for some of the anti-

557 SARS-CoV-2 mAbs described in the present study (PCT/FR2021/070522).

558 **Figure Legends**

559

560 **Figure 1. Replication kinetics of D614G, Alpha and Beta variants in cell culture.** Cells were
561 infected at the indicated MOI. Viral replication (Left) and release (Right) were assessed by flow
562 cytometry and RT-qPCR. **A)** Caco2/TC7 cells (MOI 0.01) **B)** Calu-3 cells (MOI 0.001) **C)** Vero cells
563 (MOI 0,01) **D)** primary human airway epithelial cells (HAEC) virus release (Right) and infectious
564 virus release (Left) (MOI 0.01). Data are mean \pm SD of at least 3 independent experiments.
565 Statistical analysis: Mixed-effect analysis or Two-way ANOVA compared to D614G reference, ns:
566 non-significant, *P < 0. 05, **P < 0.01, ***P < 0.001, ****P < 0.0001.

567

568 **Figure 2. SARS-CoV-2 variant infection increases formation of syncytia in U2OS-ACE2 and Vero**
569 **GFP-split cells. (A)** U2OS-ACE2 or Vero cells expressing either GFP 1-10 or GFP 11 (1:1 ratio)
570 were infected 24h after plating and imaged 20h (U2OS-ACE2) or 48h (Vero) post-infection. **(B)**
571 **Left Panel:** Fusion was quantified by GFP area/ number of nuclei and normalized to D614G for
572 U2OS-ACE2 20h post infection at MOI 0.001. **Right Panel:** Representative images of U2OS-ACE2
573 20h post infection, GFP-Split (Green) and Hoechst (Blue). Top and bottom are the same images
574 with and without Hoechst channel. **(C) Left Panel:** Quantified fusion of Vero cells infected at
575 MOI 0.01. **Right Panel:** Representative images of Vero cells 48h post infection, GFP-Split
576 (Green) and Hoechst (Blue). Scale bars: 200 μ m. Data are mean \pm SD of 8 independent

577 experiments. Statistical analysis: One-way ANOVA compared to D614G reference, ns: non-
578 significant, *P < 0.05, **P < 0.01, ***P < 0.001, ****P < 0.0001.

579

580 **Figure 3. Alpha and Beta SARS-CoV-2 S proteins induce more robust syncytia formation than**
581 **D614G. (A)** Vero GFP-split cells were transfected with variant S proteins and imaged 18h post-
582 transfection. **(B) Left Panel:** Fusion was quantified by GFP area/ number of nuclei and
583 normalized to D614G for each of the transfected variant spike proteins. **Right Panel:**
584 Representative images of Vero GFP-split cells 18h post-transfection, GFP (Green) and Hoechst
585 (Blue). Top and bottom are the same images with and without Hoechst channel. **(C) Left Panel:**
586 Quantification of variant S protein mediated fusion in Vero-GFP split cells by video microscopy.
587 Results are mean \pm SD from three fields per condition from one representative experiment.
588 **Right Panel:** Fusion quantification of at least 3 independent video microscopy experiments, 20h
589 post transfection, normalized to D614G. Scale bars: 200 μ m. Data are mean \pm SD of at least 3
590 independent experiments. Statistical analysis: One-way ANOVA compared to D614G reference,
591 ns: non-significant, *P < 0.05, **P < 0.01, ***P < 0.001, ****P < 0.0001.

592

593 **Figure 4. Mutations associated with Alpha and Beta S proteins differentially affect cell-cell**
594 **fusion. (A)** Schematic representation of the S protein colour coded for the functional regions:
595 N-terminal domain (NTD), receptor binding domain (RBD), fusion peptide (FP), heptad repeat
596 1,2 (HR1, HR2), transmembrane anchor (TA), C-terminal domain (CTD). **(B) Left Panel:** Vero

597 GFP-split cells were transfected with spike plasmids containing each of the individual mutations
598 associated with Alpha variant in the D614G background. The amount of fusion was quantified at
599 20h and normalized to D614G reference plasmid. Colour code of each mutation corresponds to
600 spike functional regions represented in (A). **Right Panel:** Quantified fusion for each of the
601 individual spike mutations associated with Beta. Data set for N501Y and D614G reference
602 mutations are duplicated between left and right panels for presentation as mutations are
603 common to both variants. **(C) Left Panel:** Quantified fusion of the Alpha + E484K variant S
604 protein normalized to D614G S. **Right Panel:** Representative images of fusion at 20h. Scale bar:
605 200 μm . Data are mean \pm SD of at least 4 independent experiments. Top and bottom are the
606 same images with and without Hoechst channel. Statistical analysis: statistics for both left and
607 right panels of A were conducted together. One-way ANOVA compared to D614G reference, ns:
608 non-significant, *P < 0.05, **P < 0.01, ***P < 0.001, ****P < 0.0001.

609

610 **Figure 5. ACE2 and monoclonal antibody binding to S proteins with Alpha and Beta associated**
611 **mutations. (A)** 293T cells were transfected S proteins with each variant-associated mutation for
612 24h and stained with biotinylated ACE2 and fluorescent streptavidin before analysis by flow
613 cytometry. **(B) Left Panel:** EC50 values (concentration of ACE2 needed for 50% binding) for
614 Alpha and associated mutations. Colour code corresponds to location on spike functional
615 domains and lower EC50 values signifies higher affinity to ACE2 binding. **Right Panel:** EC50
616 values for Beta and associated mutations. Data set for N501Y and D614G reference mutations
617 are duplicated between left and right panels as mutations are common to both variants. **(C)**

618 Spike transfected 293T cells were stained with human monoclonal antibodies targeting the S2
619 (mAb10), RBD (mAb48 and mAb98), and the NTD (mAb71). Cells were analyzed by flow
620 cytometry. The percentage of positive cells is indicated. Data are mean of at least 3
621 independent experiments. Statistical analysis: One-way ANOVA compared to D614G reference,
622 ns: non-significant, *P < 0.05, **P < 0.01, ***P < 0.001, ****P < 0.0001.

623 **Figure 6. Delta SARS-CoV-2 S protein induces more syncytia formation and binds more to**
624 **ACE2 than D614G. (A)** Vero GFP-split cells were transfected with variant S proteins and imaged
625 18h post-transfection. **Left Panel:** Fusion was quantified by GFP area/ number of nuclei and
626 normalized to D614G for each of the transfected variant spike proteins. **Right Panel:**
627 Representative images of Vero GFP-split cells 18h post-transfection, GFP (Green) and Hoechst
628 (Blue). Top and bottom are the same images with and without Hoechst channel. **(B) Left Panel:**
629 Quantification of Delta S protein mediated fusion in Vero-GFP split cells by video microscopy.
630 Results are mean \pm SD from three fields per condition from one representative experiment.
631 **Right Panel:** Fusion quantification of 3 independent video microscopy experiments, 20h post
632 transfection, normalized to D614G. **(C) 293T** cells were transfected S proteins with each variant-
633 associated mutation for 24h and stained with biotinylated ACE2 and fluorescent streptavidin
634 before analysis by flow cytometry. **Left Panel:** Representative ACE2 binding dilution curves for
635 the Delta variant in relation to Alpha and D614G. **Right Panel:** EC50 values (concentration of
636 ACE2 needed for 50% binding) for Alpha for the Delta variant. Scale bars: 200 μ m. Data are
637 mean \pm SD of at least 3 independent experiments. Statistical analysis: One-way ANOVA

638 compared to D614G reference, ns: non-significant, *P < 0.05, **P < 0.01, ***P < 0.001, ****P <
639 0.0001.

640

641

642 **Figure EV1. Assessment of viral replication by flow cytometry in cell lines (A)** Caco-2/TC7
643 (left), Calu-3 (middle), and Vero cells (right) were infected at the indicated MOIs with SARS-CoV-
644 2 variants for 24h. The number of spike protein positive cells was determined by flow
645 cytometry upon staining with human pan-SARS-CoV-2 mAb102. Only MOIs that were not
646 saturating were used to generate replication curves for each cell line studied. **(B)**
647 Representative image of gating strategy used for flow cytometry to determine spike positive
648 cells.

649

650 **Figure EV2. Qualitative and quantitative assessment of syncytia formation**

651 **(A)** U2OS-ACE2 GFP-split cells were infected at MOI 0.01 with the Wuhan, D614G, Alpha and
652 Beta strains for 20h. Cells were stained for spike protein with the human pan-SARS-CoV-2 102
653 mAb and Alex647 fluorescent secondary antibody. Representative confocal images of the
654 variant induced syncytia formation: GFP-Split (Green), Spike (red) and Hoechst (Blue). **(B)**
655 Quantification method for syncytia formation using the Opera Phenix high content imager and

656 harmony software: Total syncytia area (GFP area) is normalized for cell number upon
657 quantifying the number of nuclei (Hoechst). Scale bars: 50 μ m

658

659 **Figure EV3. Syncytia formation by SARS-CoV-2 variants (A) Left Panel:** Fusion normalized to
660 D614G for U2OS-ACE2 20h post infection at MOI 0.01. **Right Panel:** Representative images of
661 U2OS-ACE2 20h post infection, GFP (Green) and Hoechst (Blue). Top and bottom are the same
662 images with and without Hoechst channel. **(B) Left Panel:** Quantified fusion of Vero cells
663 infected at MOI 0.1. **Right Panel:** Representative images of Vero cells 48h post infection. Scale
664 bars: 200 μ m. Data are mean \pm SD of at least 3 independent experiments. Statistical analysis:
665 One-way ANOVA compared to D614G reference, ns: non-significant, *P < 0.05, **P < 0.01,
666 ***P < 0.001, ****P < 0.0001.

667 **Figure EV4. SARS-CoV-2 variant S proteins are expressed equally at the cell surface.** 293T cells
668 were transfected with variant S proteins for 20h and stained with human pan-coronavirus
669 mAb10 without permeabilization. 293T cells were chosen because they lack ACE2 and do not
670 fuse upon S transfection; this makes them suitable for single cell flow cytometry **(A) Left Panel:**
671 Quantification of percent of cells expressing each spike at the surface. **Right Panel:**
672 Representative FACs plots. **(B)** Quantification of median fluorescent intensity (MFI) of variant
673 spikes at the cell surface and representative histograms of MFI of the Wuhan, D614G, Alpha,
674 Beta, and Alpha + E484K variants spikes using mAb10. **(C)** Quantification of median fluorescent
675 intensity (MFI) of variant spikes at the cell surface and representative histograms of MFI of the
676 Wuhan, D614G, Alpha, Beta, and Alpha + E484K variants spikes using mAb129. **(D)**

677 Quantification of median florescent intensity (MFI) of variant spikes at the cell surface and
678 representative histograms of MFI of the Delta variant compared to the Alpha and D614G using
679 mAb129. **(E)** Comparison of the impact of TMPRSS2 on variant S protein processing measured
680 by western blot. Plasmids encoding for S protein were co-transfected with or without plasmids
681 expressing TMPRSS2 in 293T cells for 24h. Representative image of 2 experiments. Flow
682 cytometry data are mean \pm SD of at least 3 independent experiments. Statistical analysis: One-
683 way ANOVA compared to D614G reference, ns: non-significant, *P < 0.05, **P < 0.01, ***P <
684 0.001, ****P < 0.0001.

685

686 **Figure EV5. Impact of IFN- β 1 and IFITMs on SARS-CoV-2 variant replication and S protein**
687 **mediated cell-cell fusion.**

688 **(A)** Vero cells were pre-treated for 2h with a serial dilution of IFN- β 1 prior to infection with the
689 SARS-CoV-2 variants. Infected cells were maintained in media containing IFN- β 1 and analyzed
690 by flow cytometry 48h post-infection to determine relative infection change. **(B)** U20S-ACE2
691 GFP split cells were pre-treated for 2h with a serial dilution of IFN- β 1 prior to infection with the
692 SARS-CoV-2 variants. Infected cells were maintained in media containing IFN- β 1 and relative
693 inhibition of syncytia formation 20h post-infection was determined via GFP signal. **(C)** A co-
694 culture of 293T GFP-Split cells were transfected with combination of S, control, ACE2, TMPRSS2
695 and IFITM plasmids and then imaged 18h post-transfection. Effect of IFITMs and TMPRSS2 on
696 the cell-cell fusion induced by different spike proteins **(D)** Wuhan **(E)** D614G **(F)** Alpha **(G)** Beta.

697 Data are mean \pm SD of at least 3 independent experiments. Statistical analysis: One-way ANOVA
698 compared to D614G reference or control plasmid transfection, ns: non-significant, *P < 0.05,
699 **P < 0.01, ***P < 0.001, ****P < 0.0001.

700 **Figure EV6. SARS-CoV-2 variant S protein associated mutations are expressed equally at the**
701 **cell surface.** 293T cells were transfected with S proteins with each of the variant associated
702 mutations for 18h and stained with human pan-coronavirus mAb10 without permeabilization.
703 **(A)** Representative FACs plots of percent of cells expressing each mutant spike at the surface.
704 **(B)** Quantification of percent of cells expressing each spike at the surface. **(C)** Quantification of
705 median florescent intensity (MFI) of the mutant spikes at the cell surface. **(D)** Representative
706 histograms of MFI of each mutant spike. **(E)** Representative images of Vero GFP split cells 20h
707 after transfection with each Alpha variant associated mutant spike, GFP-Split (Green). **(F)**
708 Representative images of Vero GFP split cells 20h after transfection with each Beta variant
709 associated mutant spike. Statistical analysis: One-way ANOVA compared to D614G reference,
710 ns: non-significant, *P < 0.05, **P < 0.01, ***P < 0.001, ****P < 0.0001.

711

712 **Figure EV7. ACE2 binding curves to SARS-CoV-2 variant S proteins and associated mutations.**
713 293T cells were transfected with variant or mutant spike proteins for 24h and stained with a
714 serial dilution of soluble biotinylated ACE2 and revealed by fluorescent streptavidin before
715 analysis by flow cytometry. **(A)** ACE2 binding dilution curves of each variant spike. **(B)** ACE2
716 binding dilution curves of each variant associated mutation located in spike n-terminal domain

717 (NTD) **(C)** receptor binding domain (RBD) **(D)** S1/S2 cleavage site **(E)** heptad repeat 1-2 site
718 (HR1-HR2). Data are mean \pm SD of 3 independent experiments.

719

720 **Movie EV1: Alpha (B.1.1.7) and Beta (B.1.351) S proteins induce more robust syncytia**
721 **formation than D614G or Wuhan**

722 A co-culture of Vero GFP-split cells were transfected with plasmids expressing each of the
723 variant spike proteins and imaged by video microscopy at a rate of 6 images per hour for 24h.
724 GFP signal is superimposed over BF images. The white border represents the GFP area
725 calculated by the ImageJ macro in order to quantify fusion. **Top left:** Wuhan S **Top right:** D614G
726 S **Bottom Left:** Alpha (B.1.1.7) S **Bottom right:** Beta (B.1.351) S. One representative field for
727 each condition is shown.

728

729 **References**

- 730 Ali F, Kasry A, Amin M (2021) The new SARS-CoV-2 strain shows a stronger binding affinity to
731 ACE2 due to N501Y mutant. *Med Drug Discov* 10: 100086
- 732 Arunachalam PS, Wimmers F, Mok CKP, Perera R, Scott M, Hagan T, Sigal N, Feng Y, Bristow L,
733 Tak-Yin Tsang O *et al* (2020) Systems biological assessment of immunity to mild versus severe
734 COVID-19 infection in humans. *Science* 369: 1210-1220
- 735 Asarnow D, Wang B, Lee WH, Hu Y, Huang CW, Faust B, Ng PML, Ngoh EZX, Bohn M, Bulkley D
736 *et al* (2021) Structural insight into SARS-CoV-2 neutralizing antibodies and modulation of
737 syncytia. *Cell*
- 738 Barrett CT, Neal HE, Edmonds K, Moncman CL, Thompson R, Branttie JM, Boggs KB, Wu CY,
739 Leung DW, Dutch RE (2021) Effect of clinical isolate or cleavage site mutations in the SARS-CoV-
740 2 spike protein on protein stability, cleavage, and cell-cell fusion. *J Biol Chem* 297: 100902
- 741 Bastard P, Orlova E, Sozaeva L, Levy R, James A, Schmitt MM, Ochoa S, Kareva M, Rodina Y,
742 Gervais A *et al* (2021) Preexisting autoantibodies to type I IFNs underlie critical COVID-19
743 pneumonia in patients with APS-1. *J Exp Med* 218
- 744 Bastard P, Rosen LB, Zhang Q, Michailidis E, Hoffmann HH, Zhang Y, Dorgham K, Philippot Q,
745 Rosain J, Beziat V *et al* (2020) Autoantibodies against type I IFNs in patients with life-
746 threatening COVID-19. *Science* 370
- 747 Beucher G, Blondot M-L, Celle A, Pied N, Recordon-Pinson P, Esteves P, Faure M, Métifiot M,
748 Lacomme S, Dacheaux D *et al* (2021) SARS-CoV-2 transmission via apical syncytia release from
749 primary bronchial epithelia and infectivity restriction in children epithelia. *bioRxiv*:
750 2021.2005.2028.446159
- 751 Braga L, Ali H, Secco I, Chiavacci E, Neves G, Goldhill D, Penn R, Jimenez-Guardeno JM, Ortega-
752 Prieto AM, Bussani R *et al* (2021) Drugs that inhibit TMEM16 proteins block SARS-CoV-2 spike-
753 induced syncytia. *Nature*
- 754 Buchrieser J, Degrelle SA, Couderc T, Nevers Q, Disson O, Manet C, Donahue DA, Porrot F,
755 Hillion KH, Perthame E *et al* (2019) IFITM proteins inhibit placental syncytiotrophoblast
756 formation and promote fetal demise. *Science* 365: 176-180
- 757 Buchrieser J, Dufloo J, Hubert M, Monel B, Planas D, Rajah MM, Planchais C, Porrot F, Guivel-
758 Benhassine F, Van der Werf S *et al* (2020) Syncytia formation by SARS-CoV-2-infected cells.
759 *EMBO J* 39: e106267

- 760 Buss LF, Prete CA, Jr., Abraham CMM, Mendrone A, Jr., Salomon T, de Almeida-Neto C, Franca
761 RFO, Belotti MC, Carvalho M, Costa AG *et al* (2021) Three-quarters attack rate of SARS-CoV-2 in
762 the Brazilian Amazon during a largely unmitigated epidemic. *Science* 371: 288-292
- 763 Bussani R, Schneider E, Zentilin L, Collesi C, Ali H, Braga L, Volpe MC, Colliva A, Zanconati F,
764 Berlot G *et al* (2020) Persistence of viral RNA, pneumocyte syncytia and thrombosis are
765 hallmarks of advanced COVID-19 pathology. *EBioMedicine* 61: 103104
- 766 Cattin-Ortolá J, Welch L, Maslen SL, Skehel JM, Papa G, James LC, Munro S (2021) Sequences in
767 the cytoplasmic tail of SARS-CoV-2 Spike facilitate expression at the cell surface and syncytia
768 formation. *bioRxiv*: 2020.2010.2012.335562
- 769 Chan JF, Chan KH, Choi GK, To KK, Tse H, Cai JP, Yeung ML, Cheng VC, Chen H, Che XY *et al*
770 (2013) Differential cell line susceptibility to the emerging novel human betacoronavirus 2c
771 EMC/2012: implications for disease pathogenesis and clinical manifestation. *J Infect Dis* 207:
772 1743-1752
- 773 Chi X, Yan R, Zhang J, Zhang G, Zhang Y, Hao M, Zhang Z, Fan P, Dong Y, Yang Y *et al* (2020) A
774 neutralizing human antibody binds to the N-terminal domain of the Spike protein of SARS-CoV-
775 2. *Science* 369: 650-655
- 776 Collier DA, De Marco A, Ferreira I, Meng B, Datir RP, Walls AC, Kemp SA, Bassi J, Pinto D, Silacci-
777 Fregni C *et al* (2021) Sensitivity of SARS-CoV-2 B.1.1.7 to mRNA vaccine-elicited antibodies.
778 *Nature* 593: 136-141
- 779 Compton AA, Bruel T, Porrot F, Mallet A, Sachse M, Euvrard M, Liang C, Casartelli N, Schwartz O
780 (2014) IFITM proteins incorporated into HIV-1 virions impair viral fusion and spread. *Cell Host*
781 *Microbe* 16: 736-747
- 782 Davies NG, Abbott S, Barnard RC, Jarvis CI, Kucharski AJ, Munday JD, Pearson CAB, Russell TW,
783 Tully DC, Washburne AD *et al* (2021) Estimated transmissibility and impact of SARS-CoV-2
784 lineage B.1.1.7 in England. *Science* 372
- 785 Dittmar M, Lee JS, Whig K, Segrist E, Li M, Kamalia B, Castellana L, Ayyanathan K, Cardenas-Diaz
786 FL, Morrissey EE *et al* (2021) Drug repurposing screens reveal cell-type-specific entry pathways
787 and FDA-approved drugs active against SARS-Cov-2. *Cell Rep* 35: 108959
- 788 Dominguez SR, Travanty EA, Qian Z, Mason RJ (2013) Human coronavirus HKU1 infection of
789 primary human type II alveolar epithelial cells: cytopathic effects and innate immune response.
790 *PLoS One* 8: e70129
- 791 Duan L, Zheng Q, Zhang H, Niu Y, Lou Y, Wang H (2020) The SARS-CoV-2 Spike Glycoprotein
792 Biosynthesis, Structure, Function, and Antigenicity: Implications for the Design of Spike-Based
793 Vaccine Immunogens. *Front Immunol* 11: 576622

- 794 Edie S, Zaghloul NA, Leitch CC, Klinedinst DK, Lebron J, Thole JF, McCallion AS, Katsanis N,
795 Reeves RH (2018) Survey of Human Chromosome 21 Gene Expression Effects on Early
796 Development in *Danio rerio*. *G3 (Bethesda)* 8: 2215-2223
- 797 Ferreira I, Datir R, Papa G, Kemp S, Meng B, Rakshit P, Singh S, Pandey R, Ponnusamy K,
798 Radhakrishnan VS *et al* (2021) SARS-CoV-2 B.1.617 emergence and sensitivity to vaccine-elicited
799 antibodies. *bioRxiv*: 2021.2005.2008.443253
- 800 Frampton D, Rampling T, Cross A, Bailey H, Heaney J, Byott M, Scott R, Sconza R, Price J,
801 Margaritis M *et al* (2021) Genomic characteristics and clinical effect of the emergent SARS-CoV-
802 2 B.1.1.7 lineage in London, UK: a whole-genome sequencing and hospital-based cohort study.
803 *Lancet Infect Dis*
- 804 Franks TJ, Chong PY, Chui P, Galvin JR, Lourens RM, Reid AH, Selbs E, McEvoy CP, Hayden CD,
805 Fukuoka J *et al* (2003) Lung pathology of severe acute respiratory syndrome (SARS): a study of 8
806 autopsy cases from Singapore. *Hum Pathol* 34: 743-748
- 807 Hadjadj J, Yatim N, Barnabei L, Corneau A, Boussier J, Smith N, Pere H, Charbit B, Bondet V,
808 Chenevier-Gobeaux C *et al* (2020) Impaired type I interferon activity and inflammatory
809 responses in severe COVID-19 patients. *Science* 369: 718-724
- 810 Hoffmann M, Arora P, Gross R, Seidel A, Hornich BF, Hahn AS, Kruger N, Graichen L, Hofmann-
811 Winkler H, Kempf A *et al* (2021) SARS-CoV-2 variants B.1.351 and P.1 escape from neutralizing
812 antibodies. *Cell* 184: 2384-2393 e2312
- 813 Hoffmann M, Kleine-Weber H, Schroeder S, Kruger N, Herrler T, Erichsen S, Schiergens TS,
814 Herrler G, Wu NH, Nitsche A *et al* (2020) SARS-CoV-2 Cell Entry Depends on ACE2 and TMPRSS2
815 and Is Blocked by a Clinically Proven Protease Inhibitor. *Cell* 181: 271-280 e278
- 816 Hornich BF, Grosskopf AK, Schlagowski S, Tenbusch M, Kleine-Weber H, Neipel F, Stahl-Hennig
817 C, Hahn AS (2021) SARS-CoV-2 and SARS-CoV Spike-Mediated Cell-Cell Fusion Differ in Their
818 Requirements for Receptor Expression and Proteolytic Activation. *J Virol* 95
- 819 Hou YJ, Chiba S, Halfmann P, Ehre C, Kuroda M, Dinnon KH, 3rd, Leist SR, Schafer A, Nakajima N,
820 Takahashi K *et al* (2020) SARS-CoV-2 D614G variant exhibits efficient replication *ex vivo* and
821 transmission *in vivo*. *Science* 370: 1464-1468
- 822 Huang C, Wang Y, Li X, Ren L, Zhao J, Hu Y, Zhang L, Fan G, Xu J, Gu X *et al* (2020a) Clinical
823 features of patients infected with 2019 novel coronavirus in Wuhan, China. *Lancet* 395: 497-506
- 824 Huang Y, Yang C, Xu XF, Xu W, Liu SW (2020b) Structural and functional properties of SARS-CoV-
825 2 spike protein: potential antiviral drug development for COVID-19. *Acta Pharmacol Sin* 41:
826 1141-1149

- 827 Jackson L, Rodel H, Hwa S-H, Cele S, Ganga Y, Tegally H, Bernstein M, Giandhari J, Gosnell BI,
828 Khan K *et al* (2021) SARS-CoV-2 cell-to-cell spread occurs rapidly and is insensitive to antibody
829 neutralization. *bioRxiv*: 2021.2006.2001.446516
- 830 Jiang X, Zhang Z, Wang C, Ren H, Gao L, Peng H, Niu Z, Ren H, Huang H, Sun Q (2020) Bimodular
831 effects of D614G mutation on the spike glycoprotein of SARS-CoV-2 enhance protein
832 processing, membrane fusion, and viral infectivity. *Signal Transduct Target Ther* 5: 268
- 833 Kemp SA, Meng B, Ferriera IA, Datir R, Harvey WT, Papa G, Lytras S, Collier DA, Mohamed A,
834 Gallo G *et al* (2021) Recurrent emergence and transmission of a SARS-CoV-2 spike deletion
835 H69/V70. *bioRxiv*: 2020.2012.2014.422555
- 836 Klein S, Cortese M, Winter SL, Wachsmuth-Melm M, Neufeldt CJ, Cerikan B, Stanifer ML,
837 Boulant S, Bartenschlager R, Chlanda P (2020) SARS-CoV-2 structure and replication
838 characterized by in situ cryo-electron tomography. *Nat Commun* 11: 5885
- 839 Koch J, Uckelely ZM, Doldan P, Stanifer M, Boulant S, Lozach PY (2021) TMPRSS2 expression
840 dictates the entry route used by SARS-CoV-2 to infect host cells. *EMBO J*: e107821
- 841 Kodaka M, Yang Z, Nakagawa K, Maruyama J, Xu X, Sarkar A, Ichimura A, Nasu Y, Ozawa T, Iwasa
842 H *et al* (2015) A new cell-based assay to evaluate myogenesis in mouse myoblast C2C12 cells.
843 *Exp Cell Res* 336: 171-181
- 844 Korber B, Fischer WM, Gnanakaran S, Yoon H, Theiler J, Abfalterer W, Hengartner N, Giorgi EE,
845 Bhattacharya T, Foley B *et al* (2020) Tracking Changes in SARS-CoV-2 Spike: Evidence that
846 D614G Increases Infectivity of the COVID-19 Virus. *Cell* 182: 812-827 e819
- 847 Kreml C, Schultze B, Laude H, Herrler G (1997) Point mutations in the S protein connect the
848 sialic acid binding activity with the enteropathogenicity of transmissible gastroenteritis
849 coronavirus. *J Virol* 71: 3285-3287
- 850 Leung K, Shum MH, Leung GM, Lam TT, Wu JT (2021) Early transmissibility assessment of the
851 N501Y mutant strains of SARS-CoV-2 in the United Kingdom, October to November 2020. *Euro*
852 *Surveill* 26
- 853 Li W, Moore MJ, Vasilieva N, Sui J, Wong SK, Berne MA, Somasundaran M, Sullivan JL, Luzuriaga
854 K, Greenough TC *et al* (2003) Angiotensin-converting enzyme 2 is a functional receptor for the
855 SARS coronavirus. *Nature* 426: 450-454
- 856 Lin L, Li Q, Wang Y, Shi Y (2021) Syncytia formation during SARS-CoV-2 lung infection: a
857 disastrous unity to eliminate lymphocytes. *Cell Death Differ* 28: 2019-2021

- 858 Liu Y, Liu J, Plante KS, Plante JA, Xie X, Zhang X, Ku Z, An Z, Scharton D, Schindewolf C *et al*
859 (2021a) The N501Y spike substitution enhances SARS-CoV-2 transmission. *bioRxiv*:
860 2021.2003.2008.434499
- 861 Liu Y, Liu J, Plante KS, Plante JA, Xie X, Zhang X, Ku Z, An Z, Scharton D, Schindewolf C *et al*
862 (2021b) The N501Y spike substitution enhances SARS-CoV-2 transmission. *bioRxiv*
- 863 Liu Z, VanBlargan LA, Bloyet LM, Rothlauf PW, Chen RE, Stumpf S, Zhao H, Errico JM, Theel ES,
864 Liebeskind MJ *et al* (2021c) Identification of SARS-CoV-2 spike mutations that attenuate
865 monoclonal and serum antibody neutralization. *Cell Host Microbe* 29: 477-488 e474
- 866 Luan B, Wang H, Huynh T (2021) Molecular Mechanism of the N501Y Mutation for Enhanced
867 Binding between SARS-CoV-2's Spike Protein and Human ACE2 Receptor. *bioRxiv*:
868 2021.2001.2004.425316
- 869 Nal B, Chan C, Kien F, Siu L, Tse J, Chu K, Kam J, Staropoli I, Crescenzo-Chaigne B, Escriou N *et al*
870 (2005) Differential maturation and subcellular localization of severe acute respiratory syndrome
871 coronavirus surface proteins S, M and E. *J Gen Virol* 86: 1423-1434
- 872 Nelson G, Buzko O, Spilman P, Niazi K, Rabizadeh S, Soon-Shiong P (2021) Molecular dynamic
873 simulation reveals E484K mutation enhances spike RBD-ACE2 affinity and the combination of
874 E484K, K417N and N501Y mutations (501Y.V2 variant) induces conformational change greater
875 than N501Y mutant alone, potentially resulting in an escape mutant. *bioRxiv*:
876 2021.2001.2013.426558
- 877 Ou T, Mou H, Zhang L, Ojha A, Choe H, Farzan M (2021) Hydroxychloroquine-mediated
878 inhibition of SARS-CoV-2 entry is attenuated by TMPRSS2. *PLoS Pathog* 17: e1009212
- 879 Pizzorno A, Padey B, Julien T, Trouillet-Assant S, Traversier A, Errazuriz-Cerda E, Fouret J, Dubois
880 J, Gaymard A, Lescure FX *et al* (2020) Characterization and Treatment of SARS-CoV-2 in Nasal
881 and Bronchial Human Airway Epithelia. *Cell Rep Med* 1: 100059
- 882 Planas D, Bruel T, Grzelak L, Guivel-Benhassine F, Staropoli I, Porrot F, Planchais C, Buchrieser J,
883 Rajah MM, Bishop E *et al* (2021a) Sensitivity of infectious SARS-CoV-2 B.1.1.7 and B.1.351
884 variants to neutralizing antibodies. *Nat Med*
- 885 Planas D, Veyer D, Baidaliuk A, Staropoli I, Guivel-Benhassine F, Rajah MM, Planchais C, Porrot
886 F, Robillard N, Puech J *et al* (2021b) Reduced sensitivity of SARS-CoV-2 variant Delta to antibody
887 neutralization. *Nature*
- 888 Puray-Chavez M, LaPak KM, Schrank TP, Elliott JL, Bhatt DP, Agajanian MJ, Jasuja R, Lawson DQ,
889 Davis K, Rothlauf PW *et al* (2021) Systematic analysis of SARS-CoV-2 infection of an ACE2-
890 negative human airway cell. *Cell Rep* 36: 109364

- 891 Qian Z, Dominguez SR, Holmes KV (2013) Role of the spike glycoprotein of human Middle East
892 respiratory syndrome coronavirus (MERS-CoV) in virus entry and syncytia formation. *PLoS One*
893 8: e76469
- 894 Ramanathan M, Ferguson ID, Miao W, Khavari PA (2021) SARS-CoV-2 B.1.1.7 and B.1.351 spike
895 variants bind human ACE2 with increased affinity. *Lancet Infect Dis*
- 896 Rees-Spear C, Muir L, Griffith SA, Heaney J, Aldon Y, Snitselaar JL, Thomas P, Graham C, Seow J,
897 Lee N *et al* (2021) The effect of spike mutations on SARS-CoV-2 neutralization. *Cell Rep* 34:
898 108890
- 899 Robinot R, Hubert M, de Melo GD, Lazarini F, Bruel T, Smith N, Levallois S, Larrous F, Fernandes
900 J, Gellenoncourt S *et al* (2020) SARS-CoV-2 infection damages airway motile cilia and impairs
901 mucociliary clearance. *bioRxiv*: 2020.2010.2006.328369
- 902 Robinot R, Hubert M, de Melo GD, Lazarini F, Bruel T, Smith N, Levallois S, Larrous F, Fernandes
903 J, Gellenoncourt S *et al* (2021) SARS-CoV-2 infection induces the dedifferentiation of
904 multiciliated cells and impairs mucociliary clearance. *Nat Commun* 12: 4354
- 905 Sabino EC, Buss LF, Carvalho MPS, Prete CA, Jr., Crispim MAE, Fraiji NA, Pereira RHM, Parag KV,
906 da Silva Peixoto P, Kraemer MUG *et al* (2021) Resurgence of COVID-19 in Manaus, Brazil,
907 despite high seroprevalence. *Lancet* 397: 452-455
- 908 Sanders DW, Jumper CC, Ackerman PJ, Bracha D, Donlic A, Kim H, Kenney D, Castello-Serrano I,
909 Suzuki S, Tamura T *et al* (2021) SARS-CoV-2 requires cholesterol for viral entry and pathological
910 syncytia formation. *Elife* 10
- 911 Shi G, Kenney AD, Kudryashova E, Zani A, Zhang L, Lai KK, Hall-Stoodley L, Robinson RT,
912 Kudryashov DS, Compton AA *et al* (2021) Opposing activities of IFITM proteins in SARS-CoV-2
913 infection. *EMBO J* 40: e106501
- 914 Shi G, Schwartz O, Compton AA (2017) More than meets the I: the diverse antiviral and cellular
915 functions of interferon-induced transmembrane proteins. *Retrovirology* 14: 53
- 916 Starr TN, Greaney AJ, Addetia A, Hannon WW, Choudhary MC, Dingens AS, Li JZ, Bloom JD
917 (2021) Prospective mapping of viral mutations that escape antibodies used to treat COVID-19.
918 *Science* 371: 850-854
- 919 Tegally H, Wilkinson E, Giovanetti M, Iranzadeh A, Fonseca V, Giandhari J, Doolabh D, Pillay S,
920 San EJ, Msomi N *et al* (2020) Emergence and rapid spread of a new severe acute respiratory
921 syndrome-related coronavirus 2 (SARS-CoV-2) lineage with multiple spike mutations in South
922 Africa. *medRxiv*: 2020.2012.2021.20248640

- 923 Thorne LG, Bouhaddou M, Reuschl A-K, Zuliani-Alvarez L, Polacco B, Pelin A, Batra J, Whelan
924 MVX, Ummadi M, Rojc A *et al* (2021) Evolution of enhanced innate immune evasion by the
925 SARS-CoV-2 B.1.1.7 UK variant. *bioRxiv*: 2021.2006.2006.446826
- 926 Tian F, Tong B, Sun L, Shi S, Zheng B, Wang Z, Dong X, Zheng P (2021) Mutation N501Y in RBD of
927 Spike Protein Strengthens the Interaction between COVID-19 and its Receptor ACE2. *bioRxiv*:
928 2021.2002.2014.431117
- 929 Tian S, Hu W, Niu L, Liu H, Xu H, Xiao SY (2020) Pulmonary Pathology of Early-Phase 2019 Novel
930 Coronavirus (COVID-19) Pneumonia in Two Patients With Lung Cancer. *J Thorac Oncol* 15: 700-
931 704
- 932 Touret F, Luciani L, Baronti C, Cochin M, Driouich J-S, Gilles M, Thirion L, Nougairède A, de
933 Lamballerie X (2021) Replicative fitness SARS-CoV-2 20I/501Y.V1 variant in a human
934 reconstituted bronchial epithelium. *bioRxiv*: 2021.2003.2022.436427
- 935 van der Made CI, Simons A, Schuurs-Hoeijmakers J, van den Heuvel G, Mantere T, Kersten S,
936 van Deuren RC, Steehouwer M, van Reijmersdal SV, Jaeger M *et al* (2020) Presence of Genetic
937 Variants Among Young Men With Severe COVID-19. *JAMA* 324: 663-673
- 938 Weisblum Y, Schmidt F, Zhang F, DaSilva J, Poston D, Lorenzi JCC, Muecksch F, Rutkowska M,
939 Hoffmann HH, Michailidis E *et al* (2020) Escape from neutralizing antibodies by SARS-CoV-2
940 spike protein variants. *bioRxiv*
- 941 Xu Z, Shi L, Wang Y, Zhang J, Huang L, Zhang C, Liu S, Zhao P, Liu H, Zhu L *et al* (2020)
942 Pathological findings of COVID-19 associated with acute respiratory distress syndrome. *Lancet*
943 *Respir Med* 8: 420-422
- 944 Yadav PD, Sapkal GN, Abraham P, Ella R, Deshpande G, Patil DY, Nyayanit DA, Gupta N, Sahay
945 RR, Shete AM *et al* (2021) Neutralization of variant under investigation B.1.617 with sera of
946 BBV152 vaccinees. *bioRxiv*: 2021.2004.2023.441101
- 947 Yurkovetskiy L, Wang X, Pascal KE, Tomkins-Tinch C, Nyalile TP, Wang Y, Baum A, Diehl WE,
948 Dauphin A, Carbone C *et al* (2020) Structural and Functional Analysis of the D614G SARS-CoV-2
949 Spike Protein Variant. *Cell* 183: 739-751 e738
- 950 Zahradník J, Marciano S, Shemesh M, Zoler E, Chiaravalli J, Meyer B, Rudich Y, Dym O, Elad N,
951 Schreiber G (2021) SARS-CoV-2 RBD *in vitro* evolution follows contagious mutation
952 spread, yet generates an able infection inhibitor. *bioRxiv*: 2021.2001.2006.425392
- 953 Zani A, Yount JS (2018) Antiviral Protection by IFITM3 In Vivo. *Curr Clin Microbiol Rep* 5: 229-237
- 954 Zhang X, Tan Y, Ling Y, Lu G, Liu F, Yi Z, Jia X, Wu M, Shi B, Xu S *et al* (2020) Viral and host factors
955 related to the clinical outcome of COVID-19. *Nature* 583: 437-440

- 956 Zhang Z, Zheng Y, Niu Z, Zhang B, Wang C, Yao X, Peng H, Franca DN, Wang Y, Zhu Y *et al* (2021)
957 SARS-CoV-2 spike protein dictates syncytium-mediated lymphocyte elimination. *Cell Death*
958 *Differ*
- 959 Zhou H, Chen Y, Zhang S, Niu P, Qin K, Jia W, Huang B, Zhang S, Lan J, Zhang L *et al* (2019)
960 Structural definition of a neutralization epitope on the N-terminal domain of MERS-CoV spike
961 glycoprotein. *Nat Commun* 10: 3068
- 962 Zhou Z, Ren L, Zhang L, Zhong J, Xiao Y, Jia Z, Guo L, Yang J, Wang C, Jiang S *et al* (2020)
963 Heightened Innate Immune Responses in the Respiratory Tract of COVID-19 Patients. *Cell Host*
964 *Microbe* 27: 883-890 e882
- 965 Zhu N, Wang W, Liu Z, Liang C, Wang W, Ye F, Huang B, Zhao L, Wang H, Zhou W *et al* (2020)
966 Morphogenesis and cytopathic effect of SARS-CoV-2 infection in human airway epithelial cells.
967 *Nat Commun* 11: 3910

968

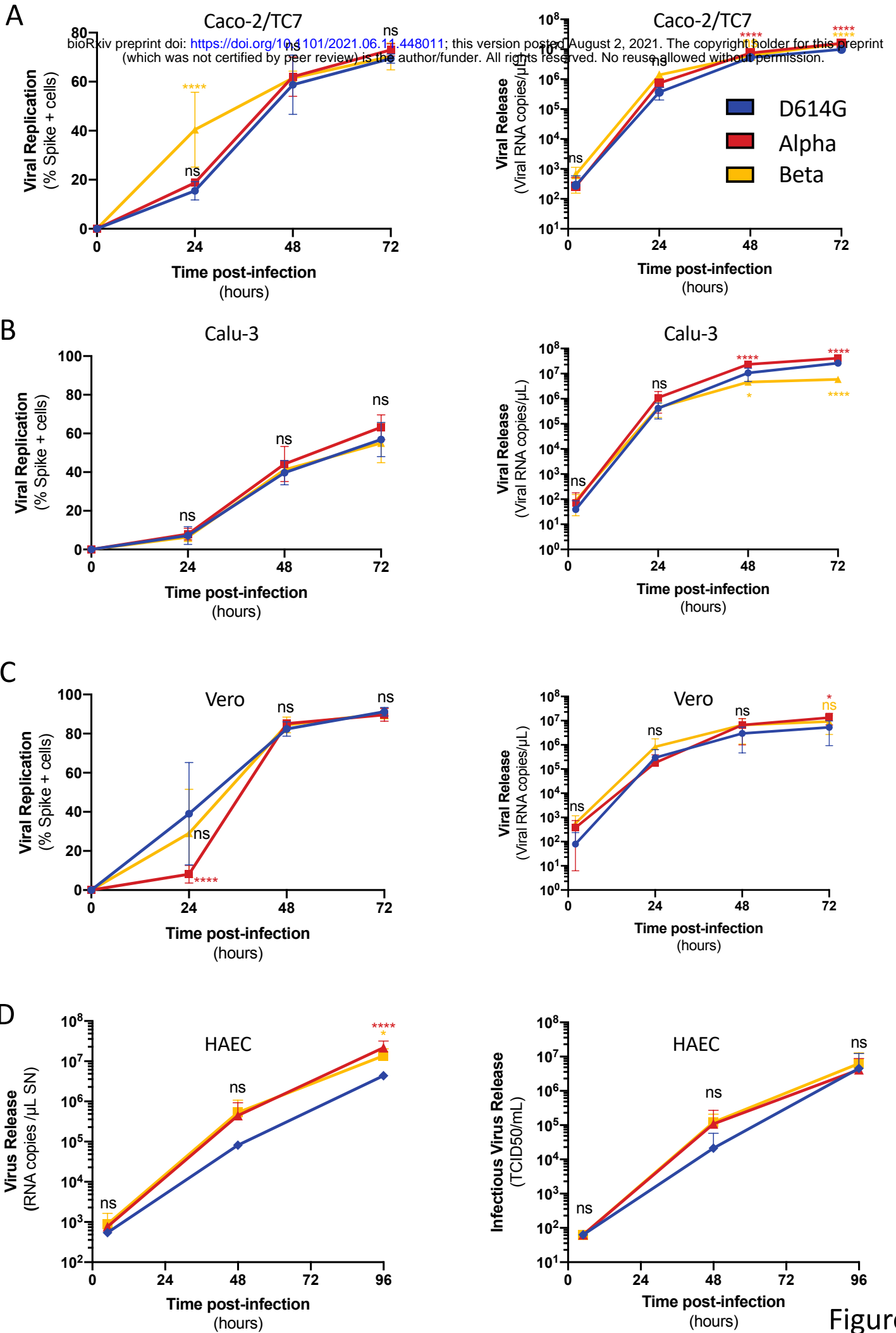
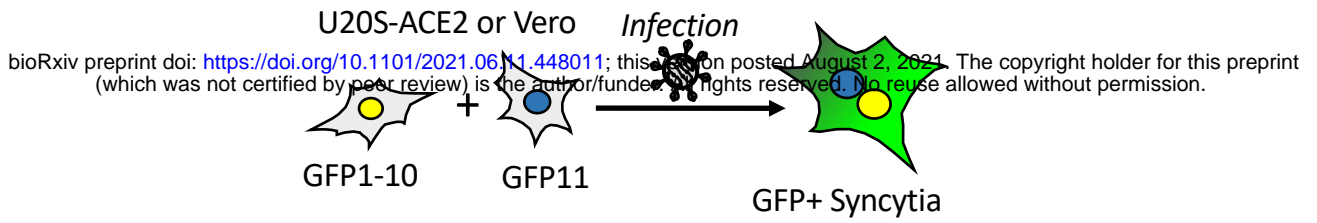
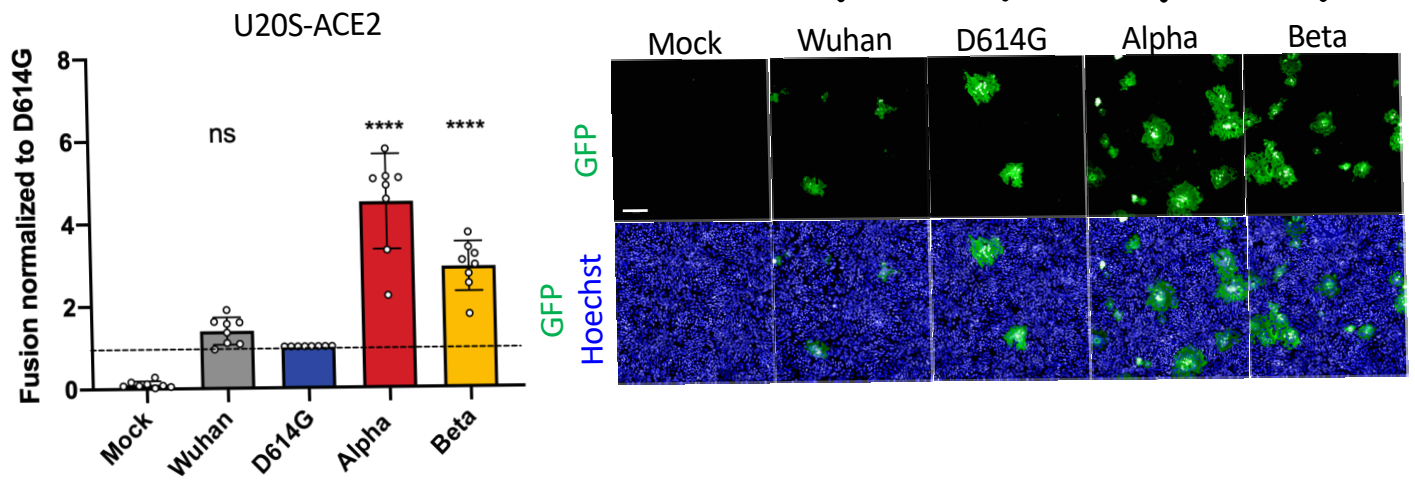


Figure 1

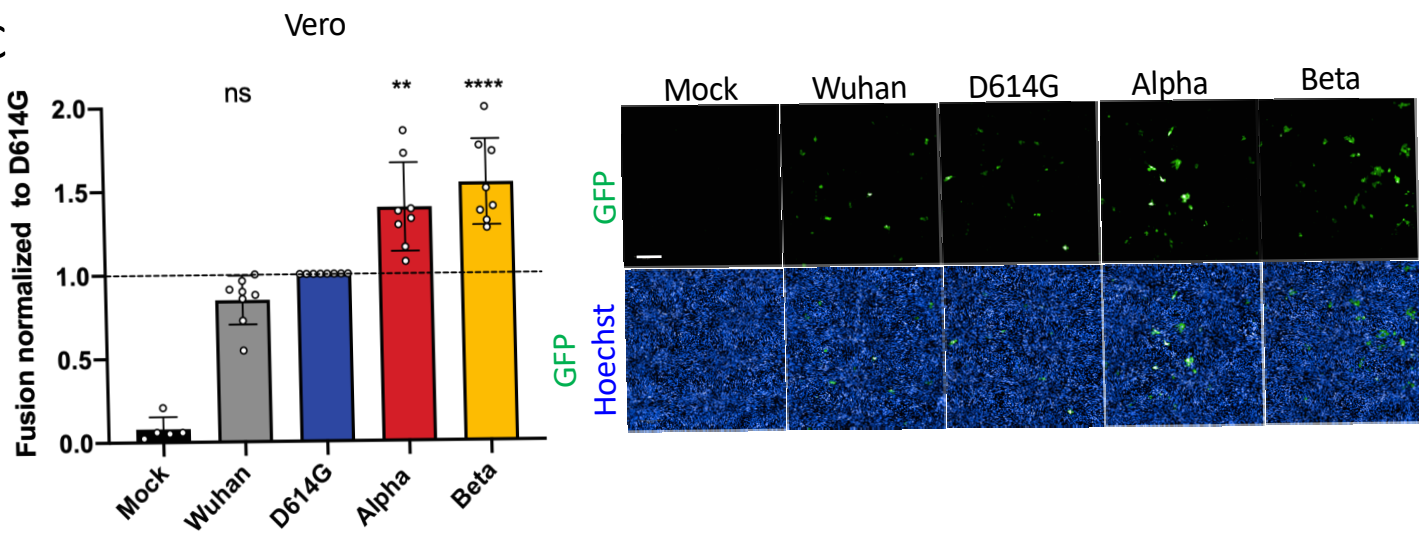
A



B

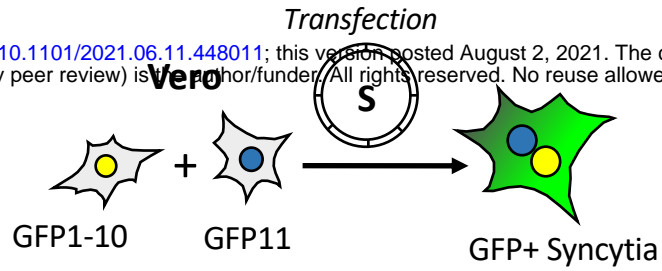


C

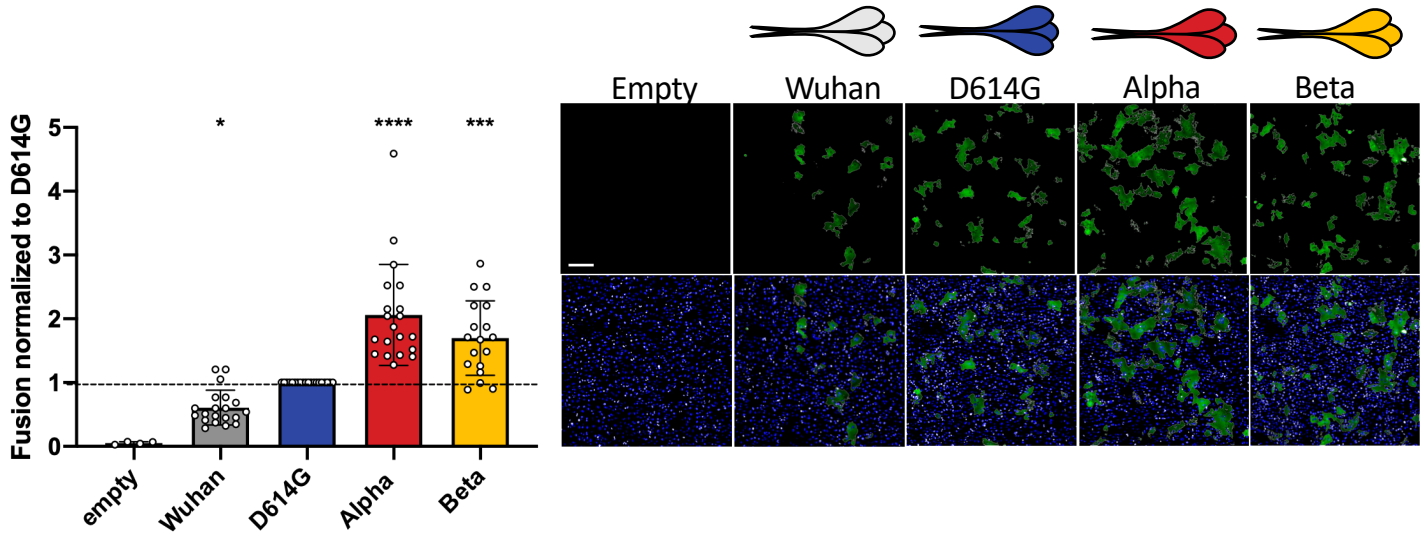


A

bioRxiv preprint doi: <https://doi.org/10.1101/2021.06.11.448011>; this version posted August 2, 2021. The copyright holder for this preprint (which was not certified by peer review) is the author/funder. All rights reserved. No reuse allowed without permission.



B



C

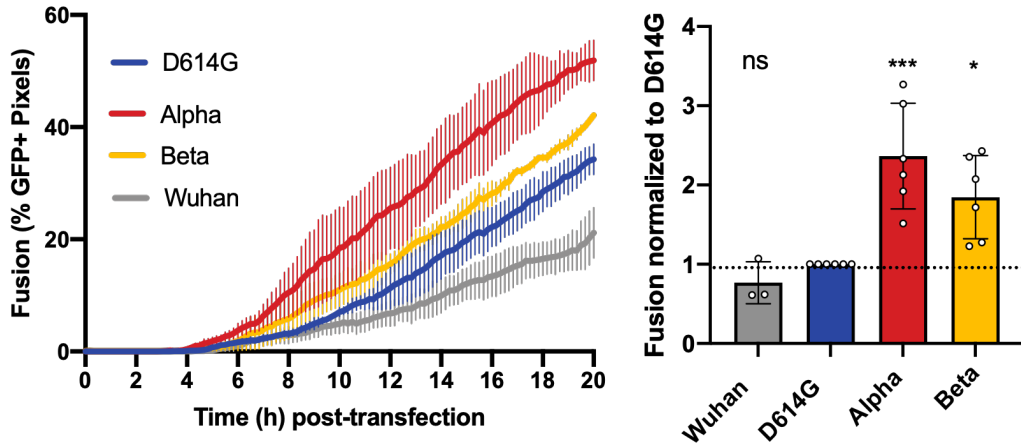
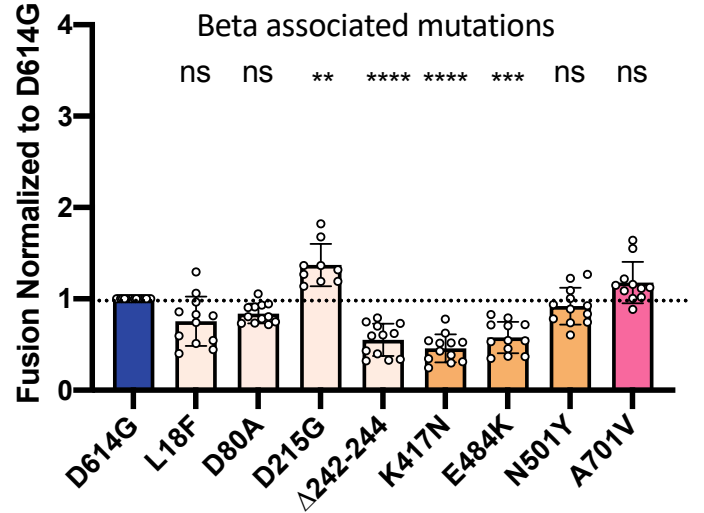
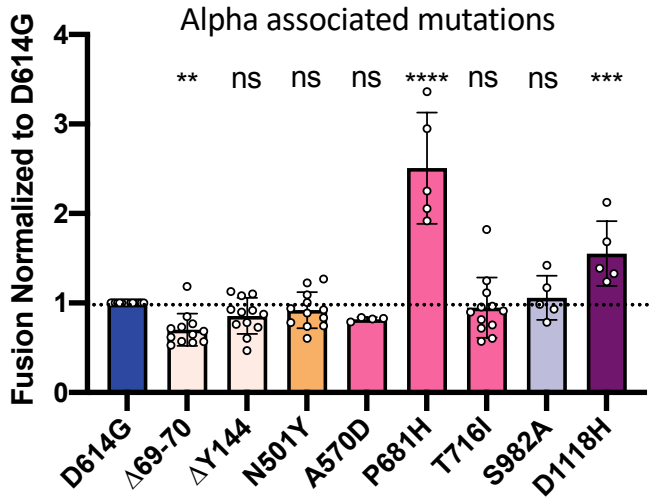
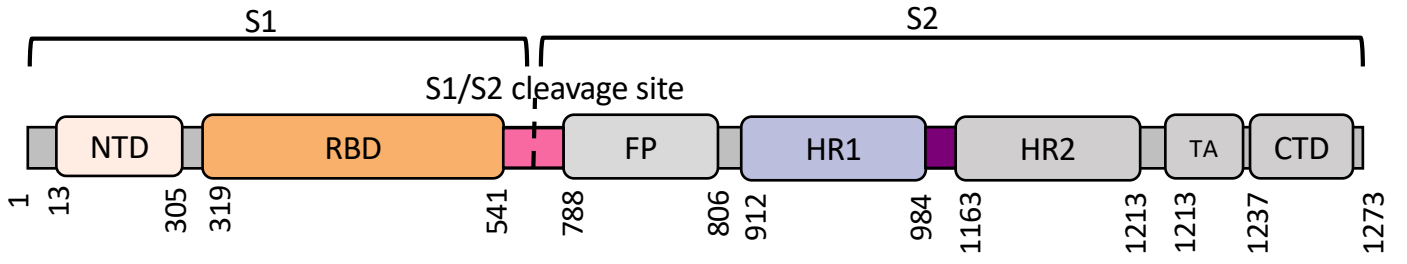


Figure 3

A



B

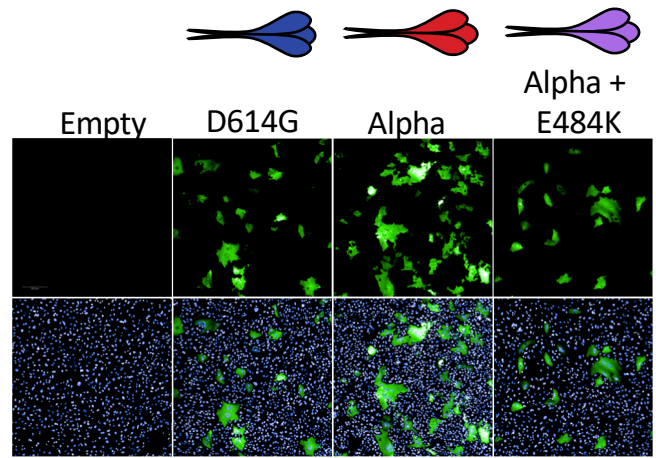
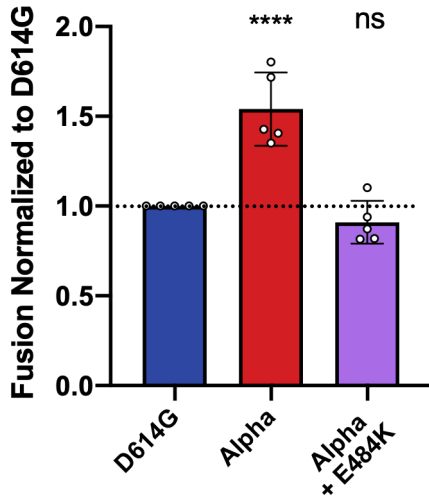


Figure 4

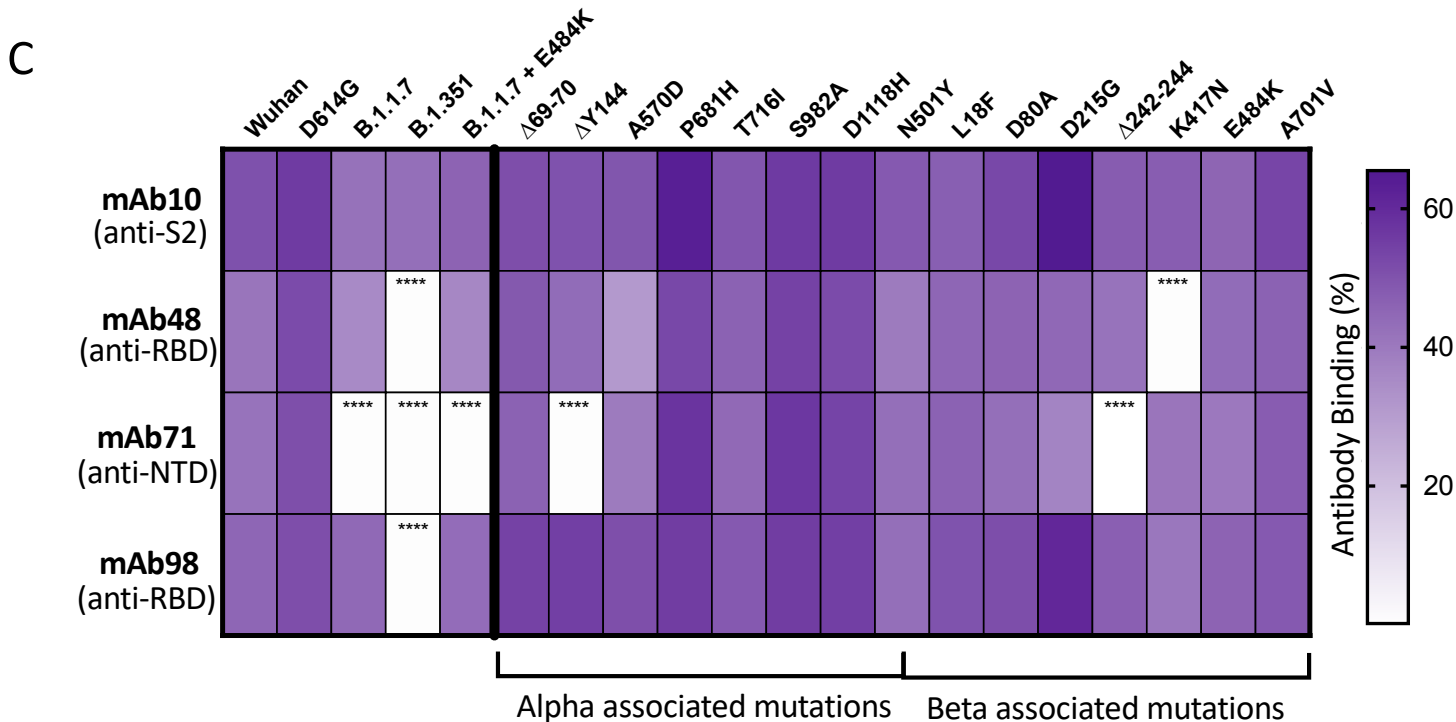
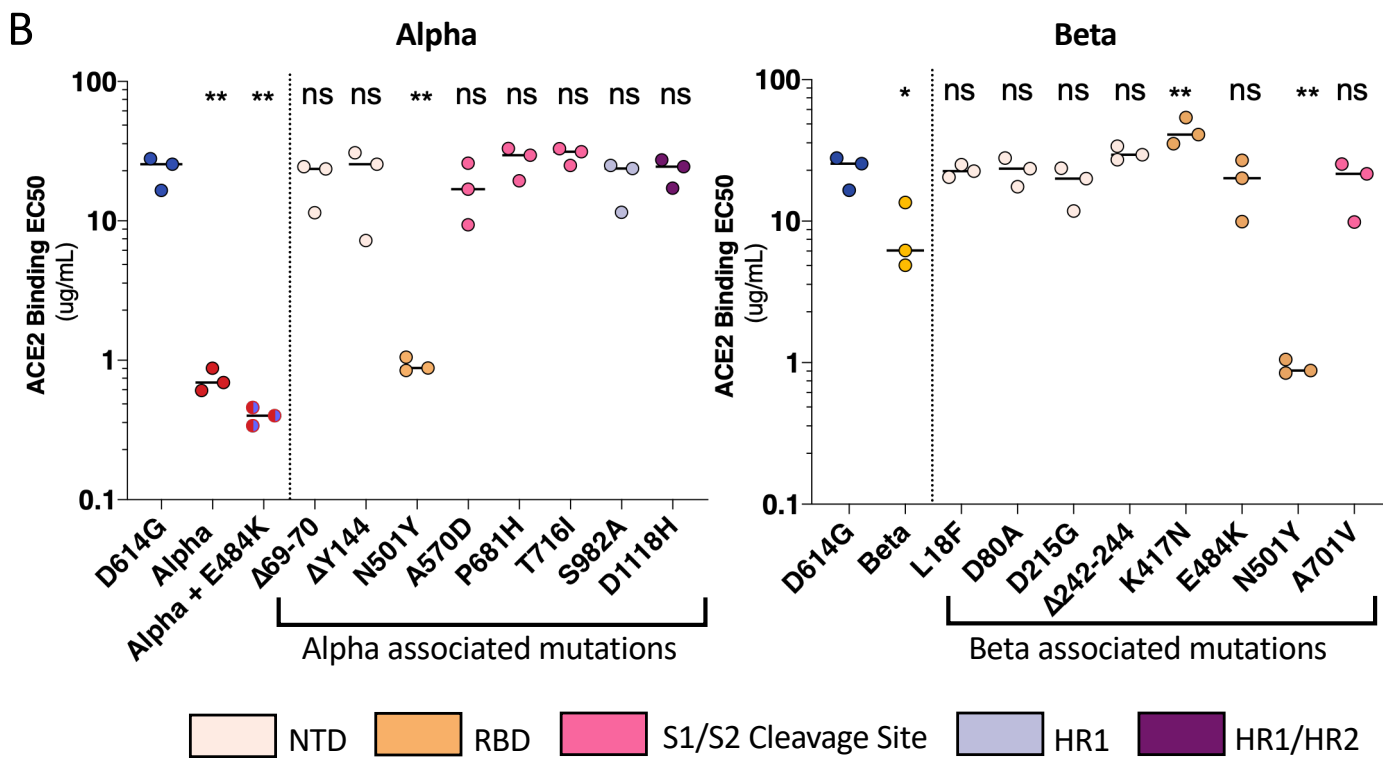
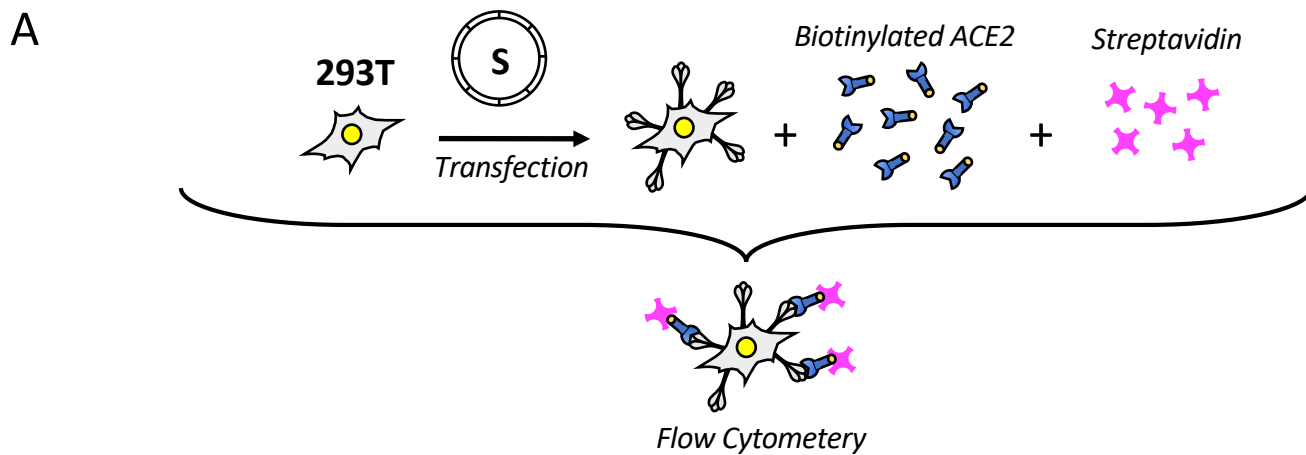
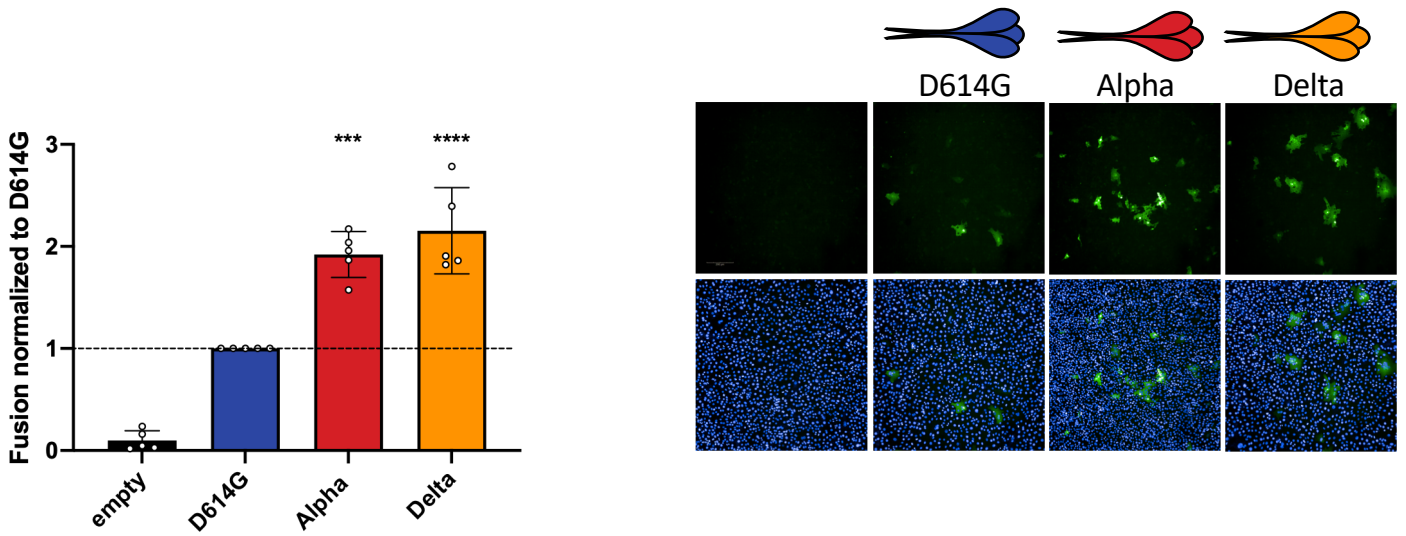
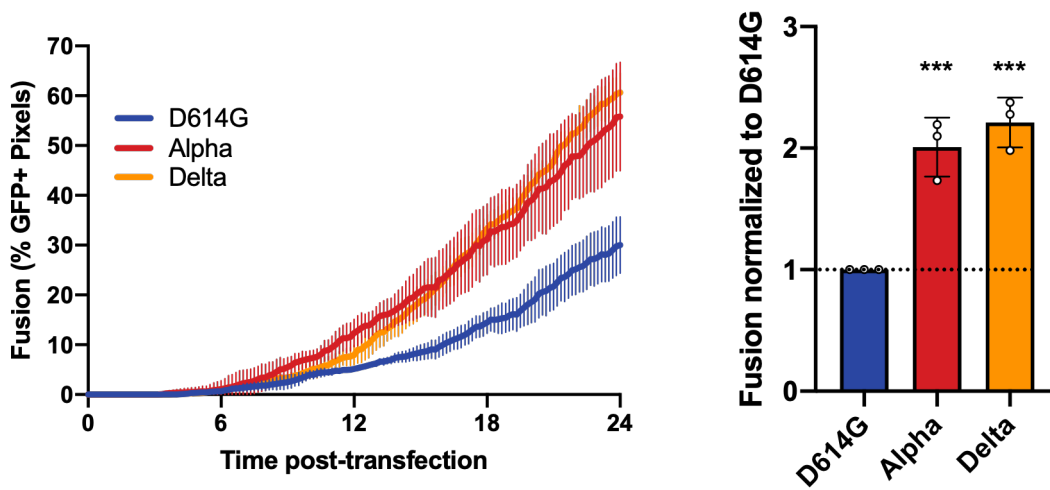


Figure 5

A



B



C

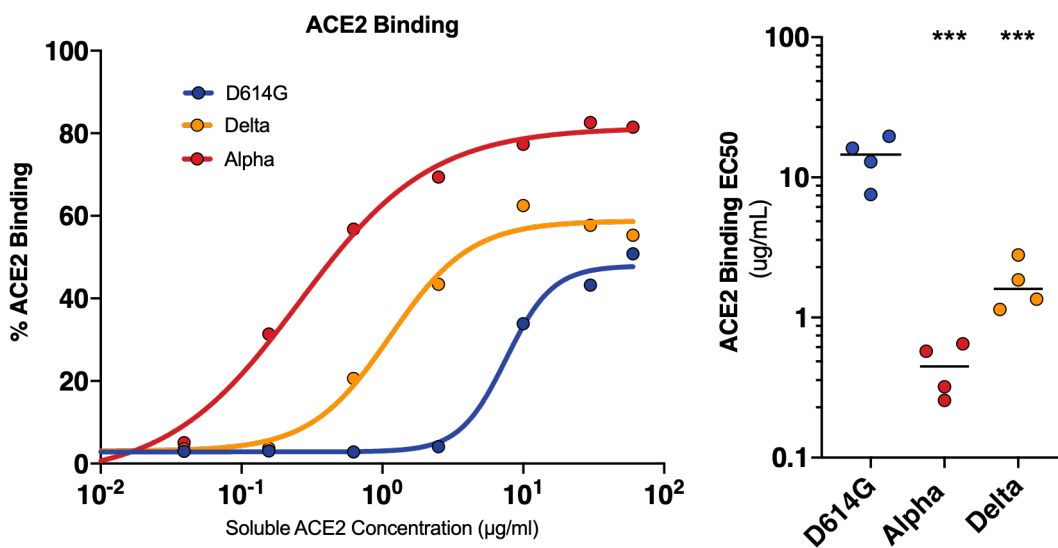
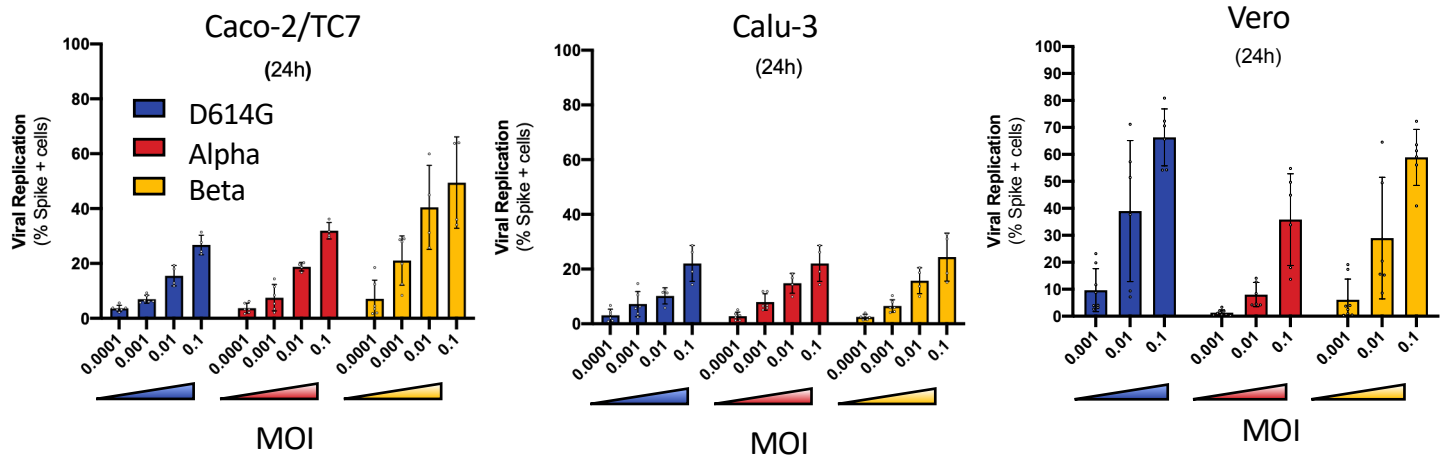
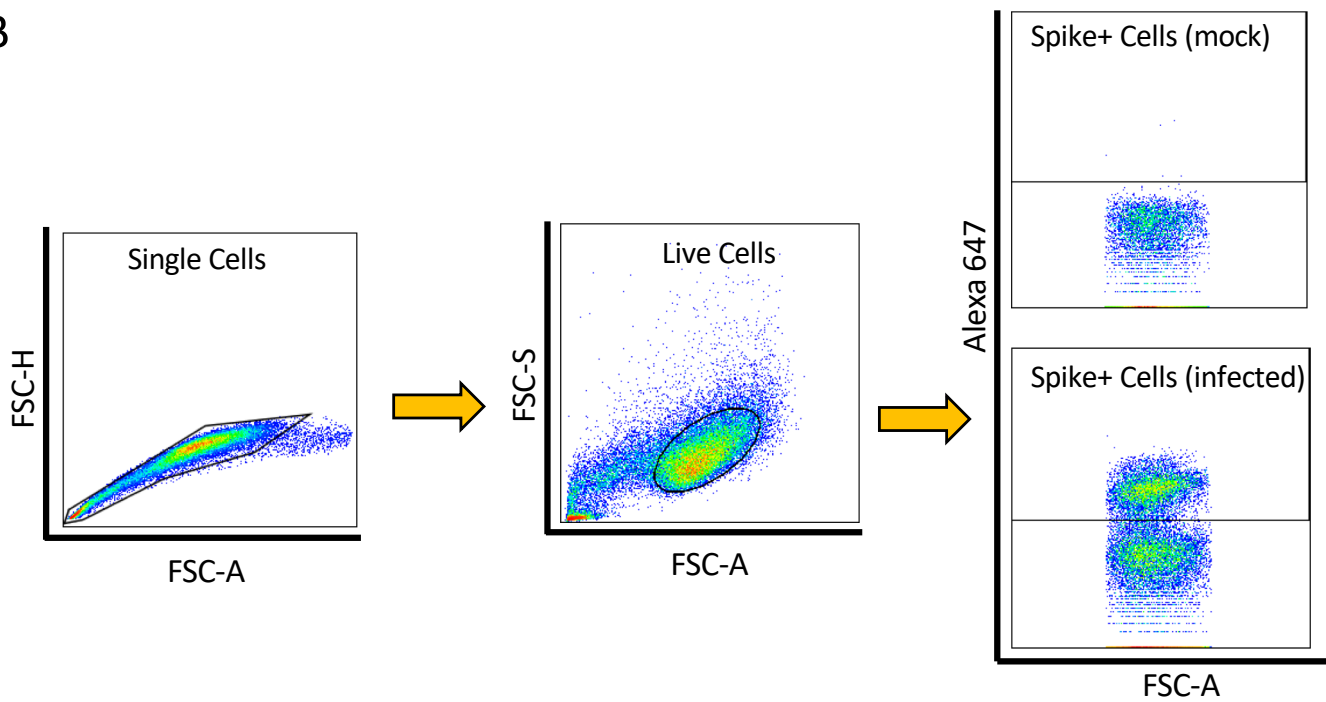


Figure 6

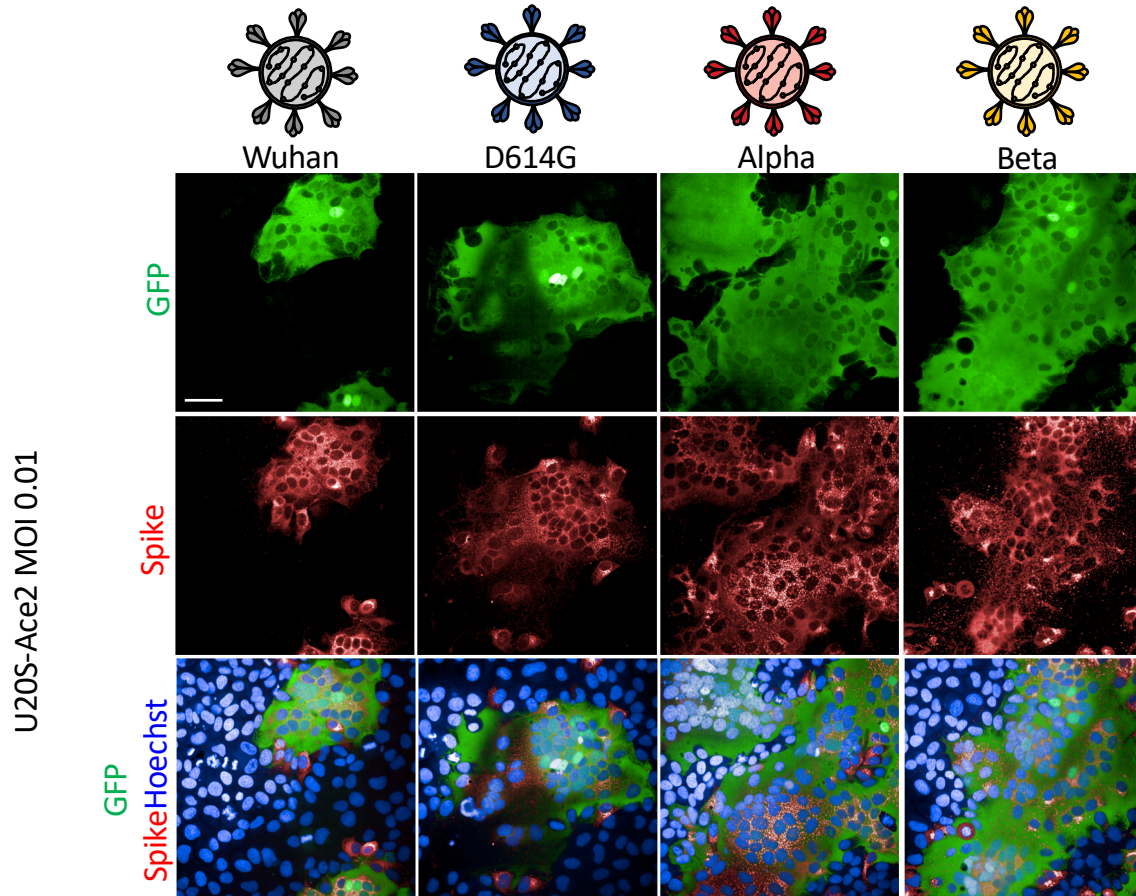
A



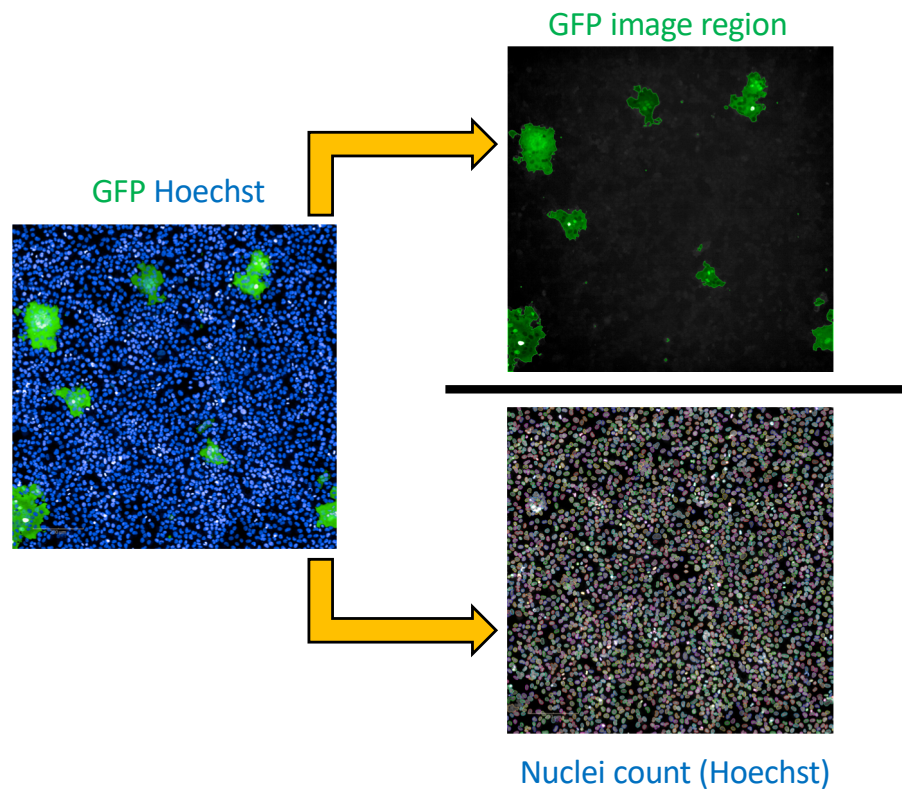
B



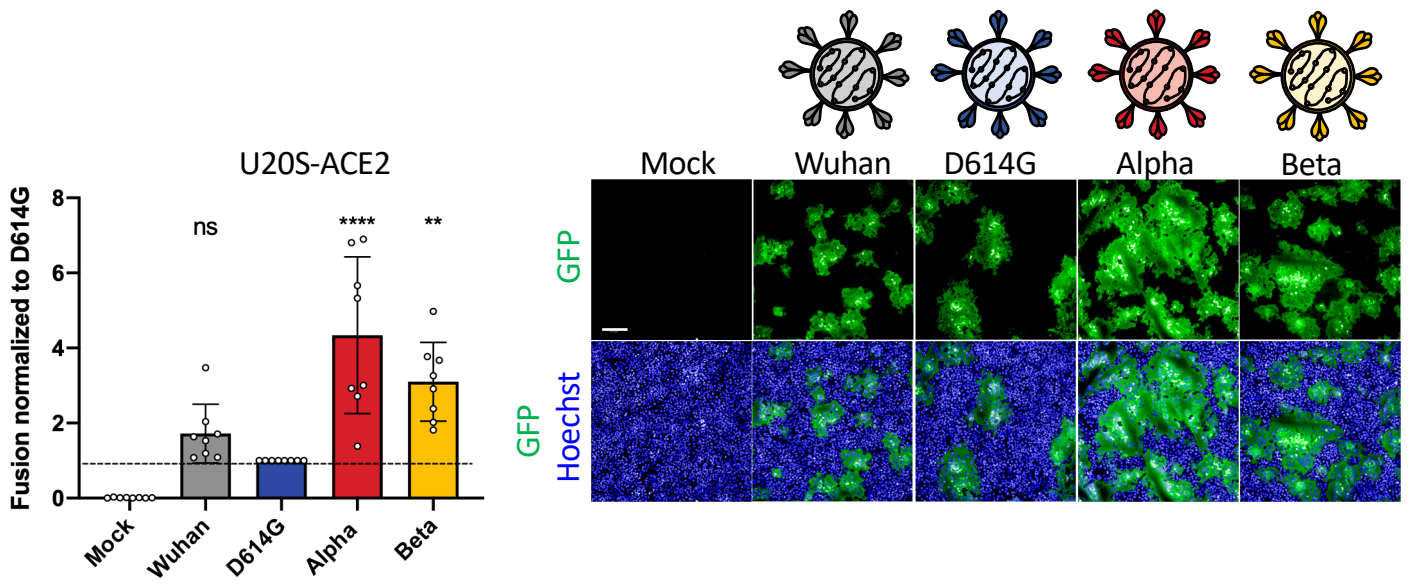
A



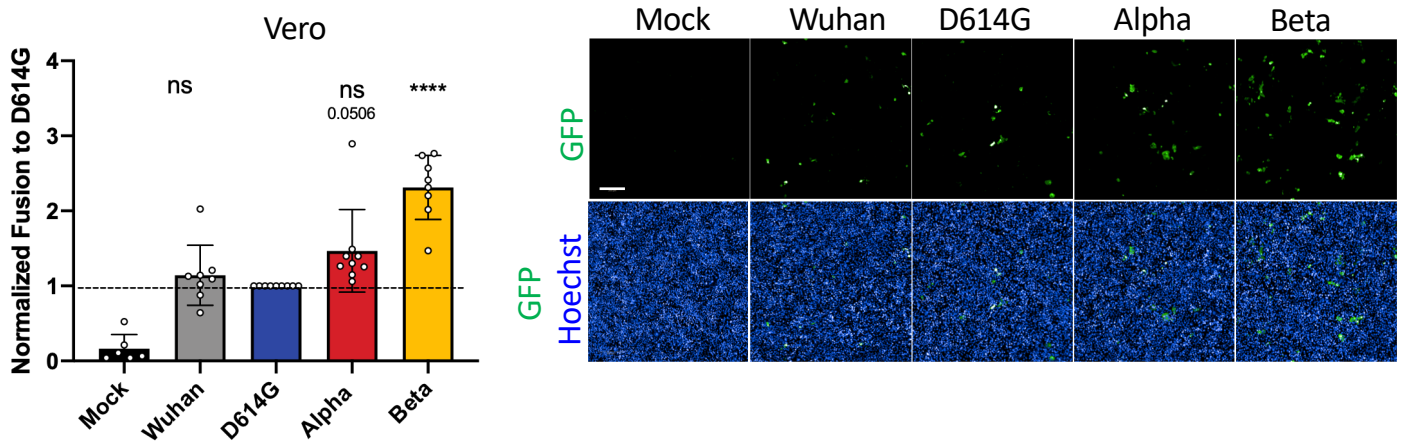
B

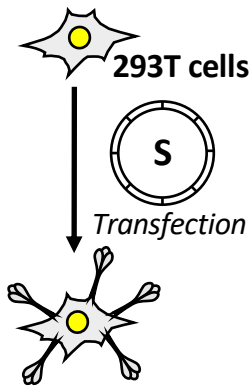


A

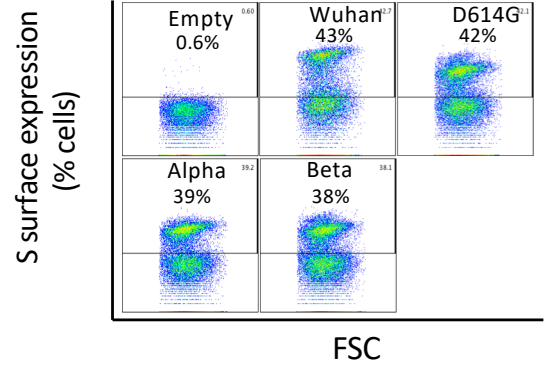
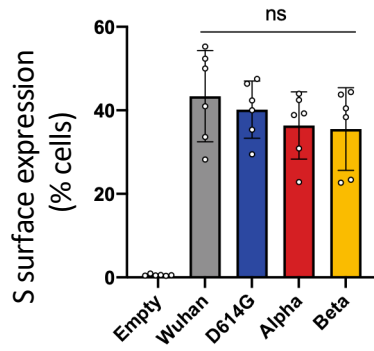


B

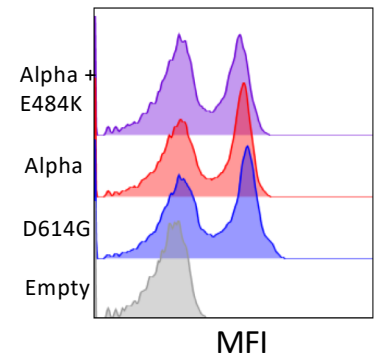
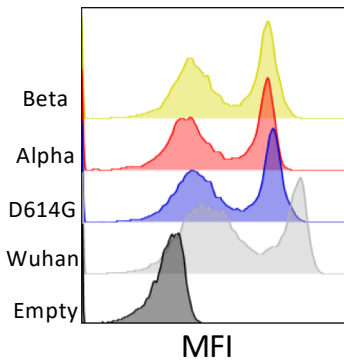
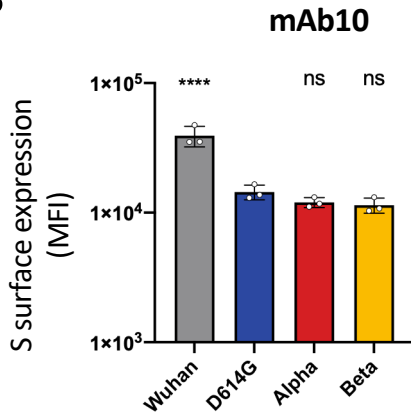




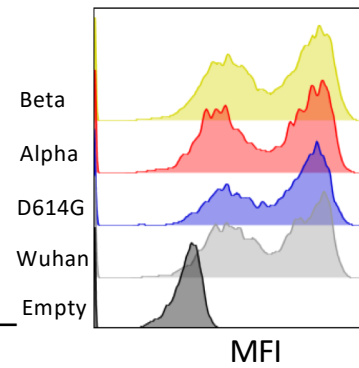
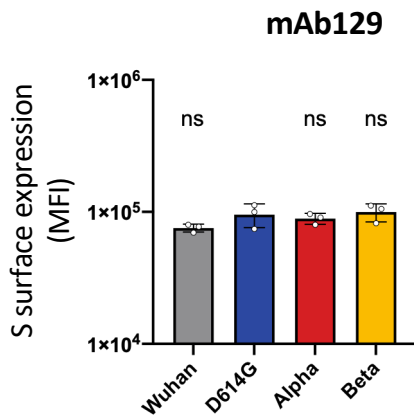
A



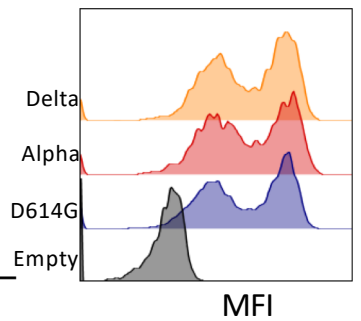
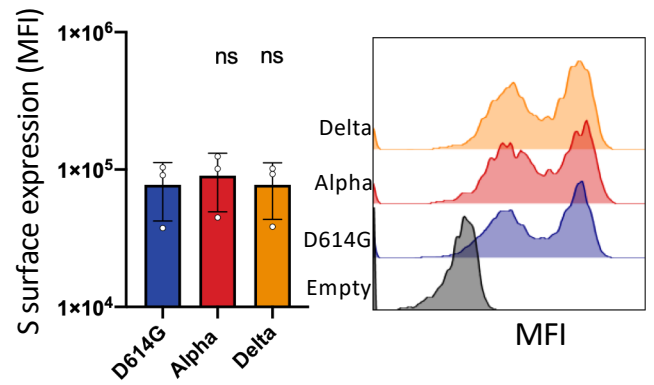
B



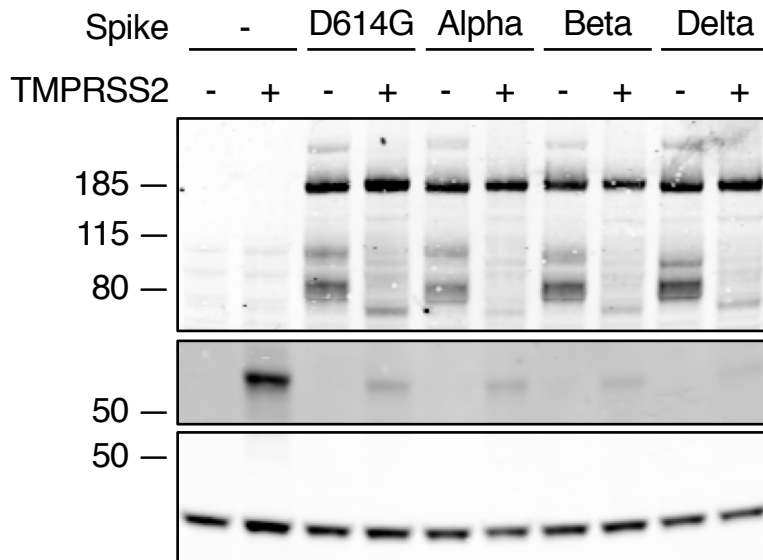
C



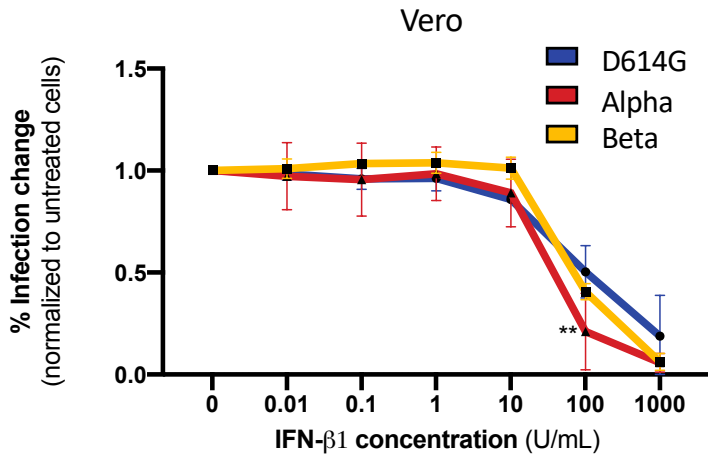
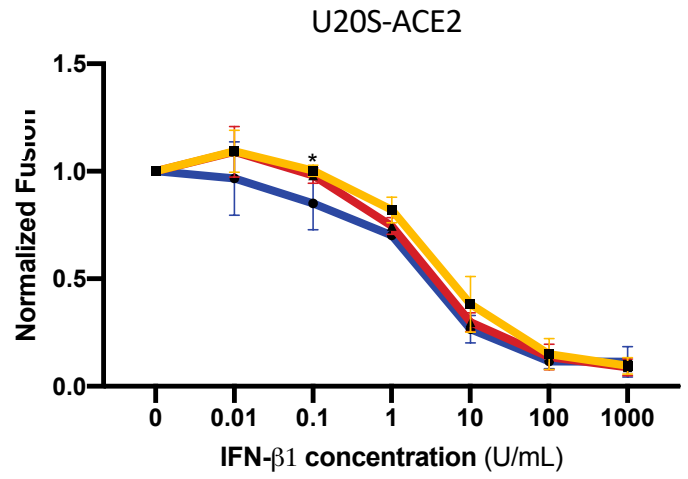
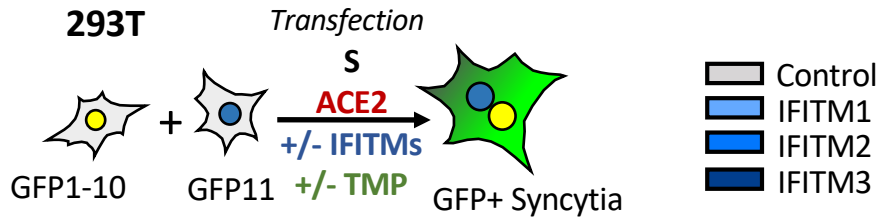
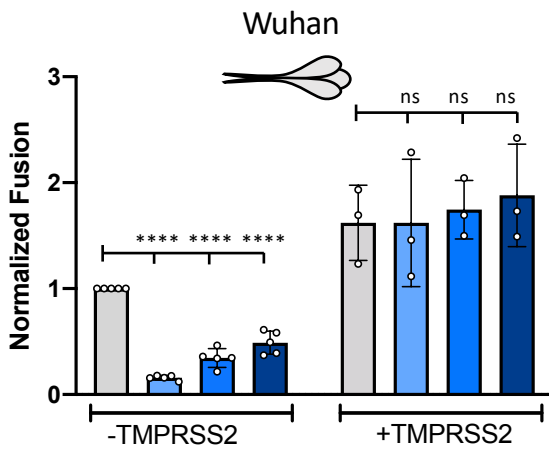
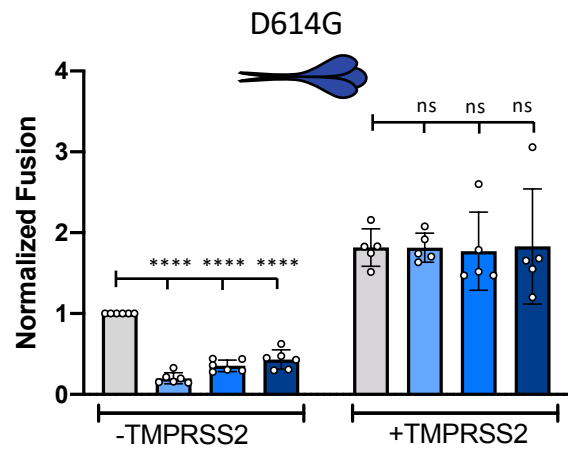
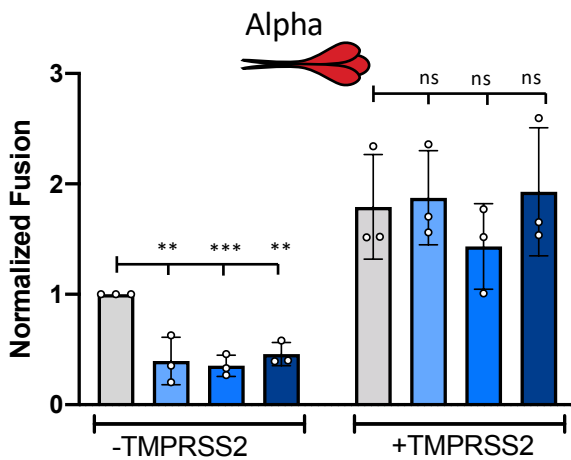
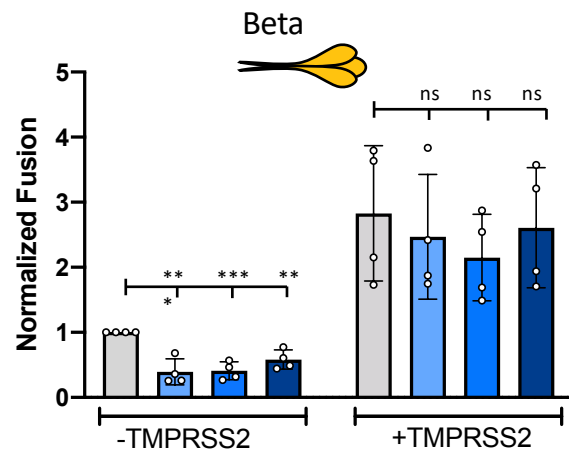
D

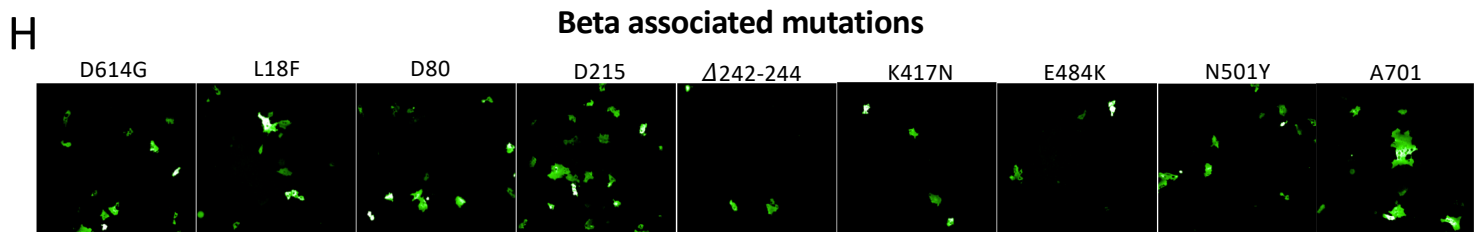
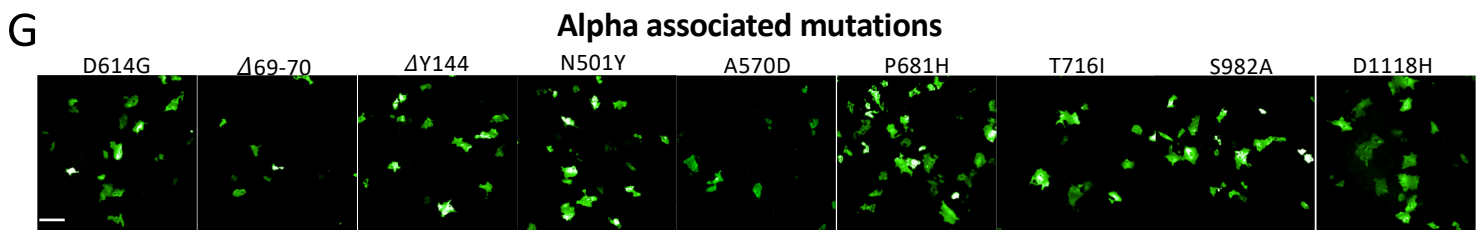
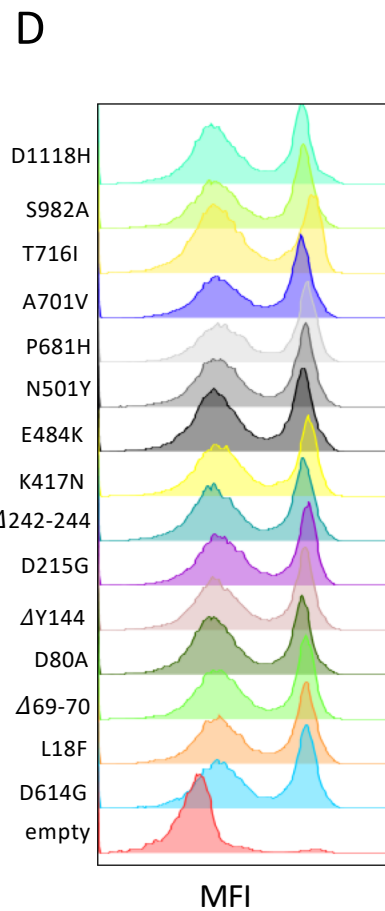
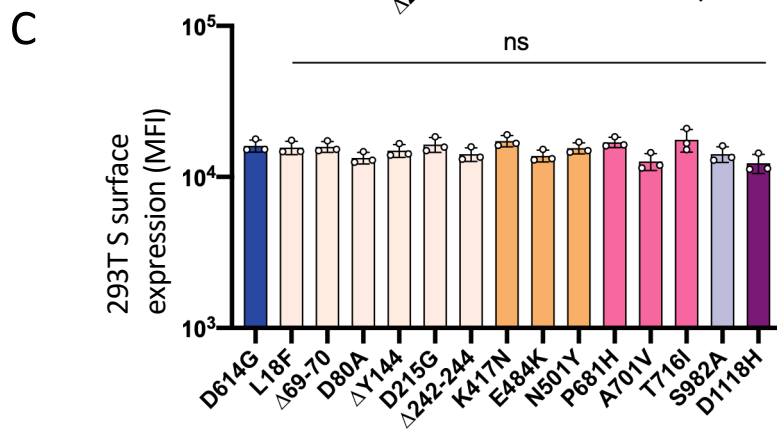
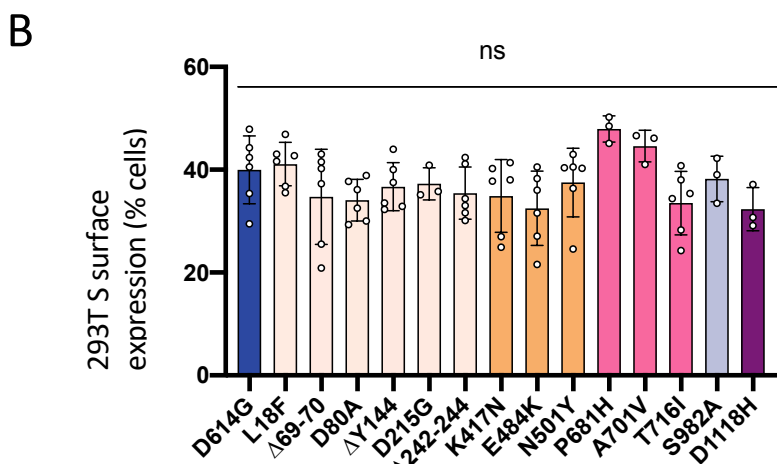
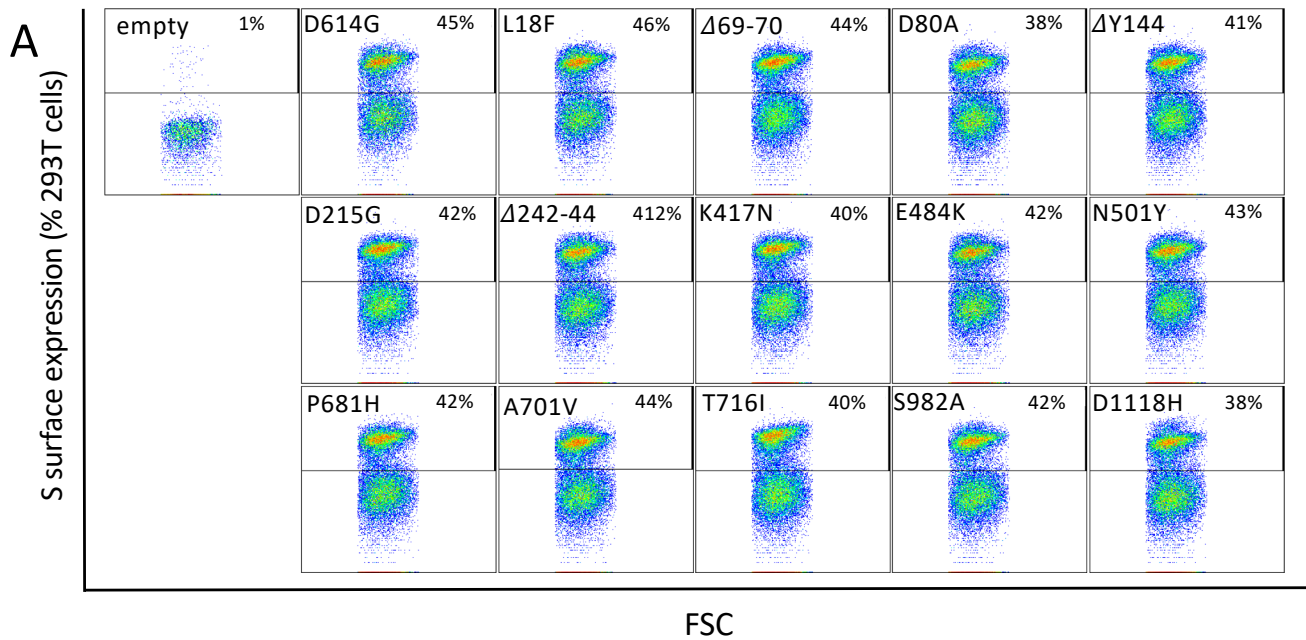


E

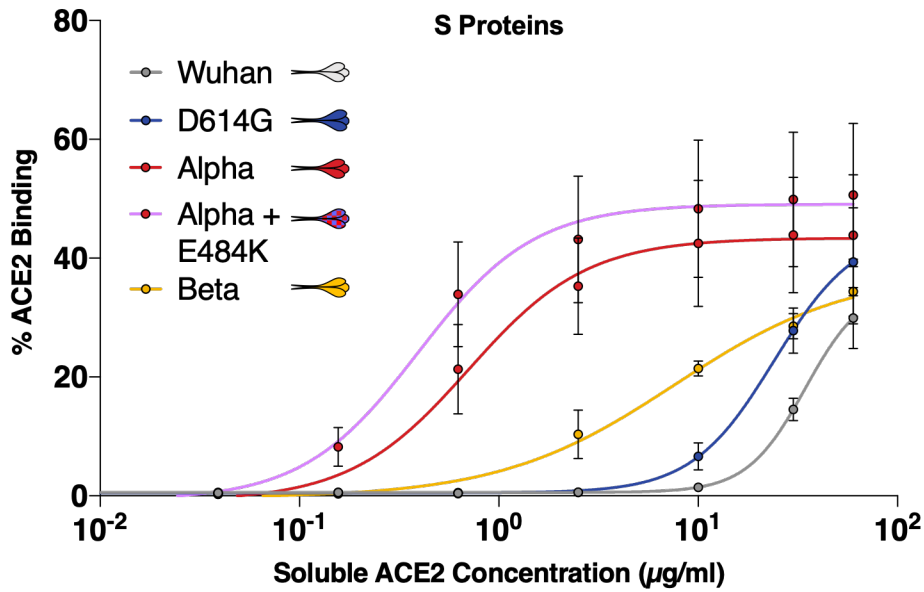


Expanded View 4

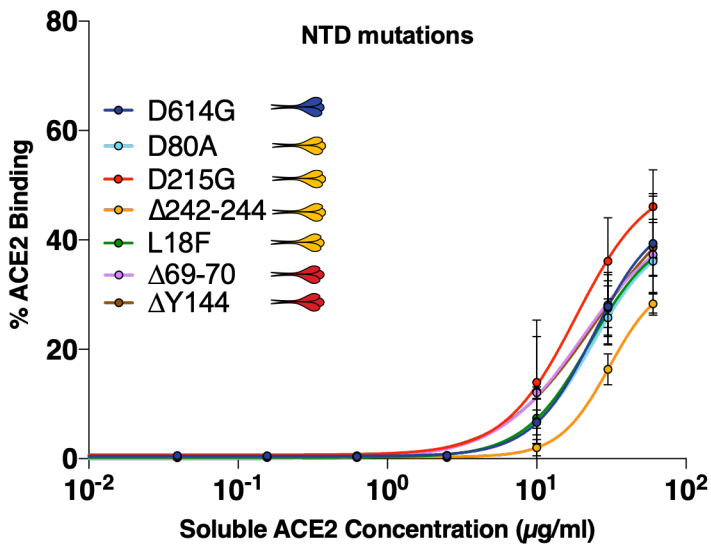
A**B****C****D****E****F****G**



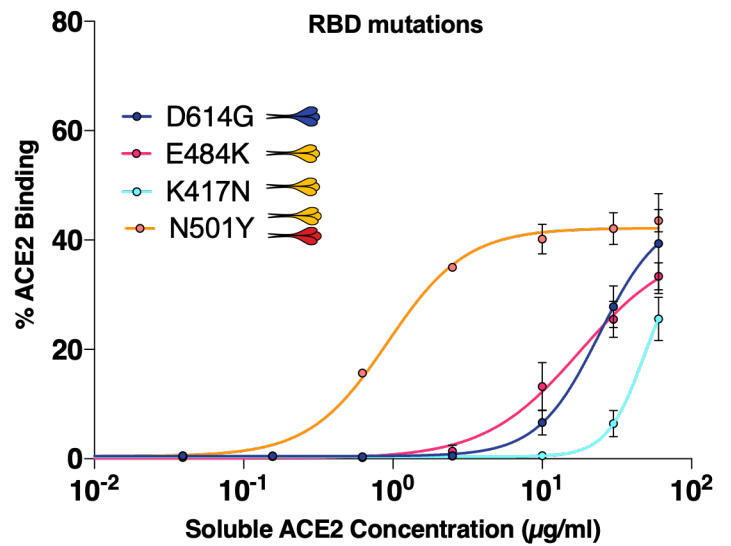
A



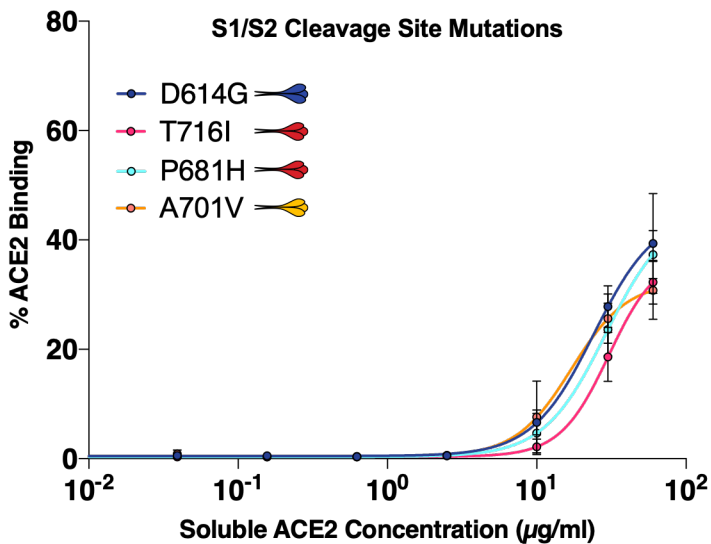
B



C



D



E

